LATVIAN JOURNAL of PHYSICS and TECHNICAL SCIENCES

ISSN 0868 - 8257

1-2

(Vol. 57)

2020

CONTENTS

LATVIAN JOURNAL of PHYSICS and TECHNICAL SCIENCES

LATVIJAS FIZIKAS un TEHNISKO ZINĀTŅU ŽURNĀLS

ЛАТВИЙСКИЙ ФИЗИКО-ТЕХНИЧЕСКИЙ ЖУРНАЛ

Published six times a year since February 1964
Iznāk sešas reizes gadā kopš 1964. gada februāra
Выходит шесть раз в год с февраля 1964 года

1-2 (Vol. 57) • 2020

RĪGA

EDITORIAL BOARD

N. Zeltins (Editor-in-Chief), A. Sternbergs (Deputy Editor-in-Chief),
A. Ozols, A. Mutule, J. Kalnacs, A. Silins, G. Klavs, A. Sarakovskis,
M. Rutkis, A. Kuzmins, E. Birks, L. Jansons (Managing Editor)

ADVISORY BOARD

L. Gawlik (Poland), T. Jeskelainen (Sweden), J. Melngailis (USA),
J. Savickis (Latvia), K. Schwartz (Germany), A. Zigurs (Latvia)

Language Editor: O. Ivanova
Computer Designer: I. Begicevs

INDEXED (PUBLISHED) IN

www.scopus.com
www.sciendo.com
EBSCO (Academic Search Complete, www.epnet.com), INSPEC (www.iee.org.com).
VINITI (www.viniti.ru), Begell House Inc/ (EDC, www.edata-center.com).

Issuers: Institute of Physical Energetics,
Institute of Solid State Physics, University of Latvia
Registration Certificate Number: 000700221

Editorial Contacts:
11 Krivu Street, Riga, LV - 1006
Ph.: + 371 67551732
E-mail: leo@lza.lv
www.fei-web.lv

sciendo

LATVIAN JOURNAL OF PHYSICS
AND TECHNICAL SCIENCES
2020, N 1-2

BALTIC APPLIED ASTROINFORMATICS AND SPACE DATA PROCESSING 2019

The 6th International Scientific Conference "Baltic Applied Astroinformatics and Space data Processing 2019" (BAASP'2019) was held on 21–23 August 2019 at Ventspils University of Applied Sciences and organised by the Engineering Research Institute "Ventspils International Radio Astronomy Centre" (VIRAC) of Ventspils University of Applied Sciences. The Conference was dedicated to the 25th anniversary of the VIRAC.

The event saw a record number of participants who attended the Conference in 2019 – 55 participants, who made a total of 43 scientific presentations. The Conference was divided into 6 parallel scientific sessions: Galactic Astronomy, Remote Sensing, Research of Sun Studies, Data Processing Methods, Extragalactic Astronomy, Instrumentation for Space Technologies and VLBI Methods. Organisers invited six world-class scientists to be keynote speakers – Leonid Gurvits (NL), Dmitry Wiebe (RUS), Vasily Beskin (RUS), Oleg Ulyanov (UKR), Gino Tuccari (ITA) and Francisco Colomer (NL). In their presentations, they talked about future applications of VLBI technology, radio pulsars, evolution of astrochemistry and the planets, low-frequency radio astronomical instrumentation and its data processing techniques. The Conference was attended by scientists from eight countries – Latvia, Estonia, Italy, Sweden, Finland, the Netherlands, Russia and Ukraine.

The top 20 scientific articles are planned to be published in two journals, articles on the development of scientific instruments will be published in the Latvian Journal of Physics and Technical Sciences and articles on research in fundamental astronomy and astrophysics will be published in Astronomical and Astrophysical Transactions.

Conference Theme

Space science is being fundamentally influenced and empowered by computation and information technology, and it stimulates further technological developments. Astronomy, like many other fields, is becoming exponentially data-rich, and the tasks of data management, data acquisition, and knowledge discovery become central to our research organisation, bringing together many technical and methodological challenges. Information technology also provides the stage where we collaborate and interact, and publish, preserve, use and disseminate knowledge. The general philosophy behind is to be future-oriented, which determines the emerging discipline of astroinformatics.

Recent challenges are directed towards more human-oriented, highly personalized and trustworthy systems enabling their users to cope with a large variety of frameworks, technologies, data volumes and tools needed to accommodate emerging scientific applications. Therefore, one of the areas of focus here is quantitative and qualitative methods for exploiting, predicting, and understanding the value that the state-of-the-art information and communication technologies bring to space science, astronomy, geodesy and related fields.

The scope of the Conference covers fundamental and applied research that is related to space technologies and includes the following:

- SPACE SCIENCE, including space and atmospheric physics, Earth observation and remote sensing from space, planetary sciences, astrochemistry, space geodesy, astronomy and astrophysics;
- SPACE ENGINEERING, including communications, navigation, space operations, satellite design, testing, and implementation, engineering of new generation radio telescope frontend and backend solutions;
- SPACE AND INDUSTRIAL IT SOLUTIONS, including data acquisition, signal processing, data correlation, data recording, transfer, processing and archiving high performance and cloud computing techniques.

The Aim of the Conference

The Conference is a collaboration platform for cross-border partnership and knowledge transfer for astronomers, astrophysicists, space researchers and engineers, as well as for experts in related research disciplines such as informatics, electronics, satellite technology, geodesy and environment sciences. While the general scope of BAASP is wide, the specific themes of BAASP'2019 are astrophysics, space technologies and remote sensing.

A KEY FOCUS IN 2019

Astrophysics, Remote Sensing and New Generation Radio Electronics

The Conference was planned in six parallel sessions:

- Astrophysics is driven by the exploitation of astronomical observations, which includes data processing, interpretation, and putting the results in an appropriate scientific context to understand the underlying physical phenomena. The path from observations to discoveries was the focus of BAASP'2019.
- Remote sensing is another example, where technologically complex investment ultimately yields scientific and commercially useful results. Besides observations of the Earth, it also includes the Moon and other planets, satellites, even comets, and asteroids in the Solar system. With BAASP'2019, we aimed to promote a discussion on aspects of data processing and interpretation in remote sensing.

- New generation radio electronics is the basis of new discoveries in astrophysics and radio astronomy since novel technology implementations of new modern radio systems enhance the properties of current radioastronomy instrumentation, thus improving specific observing capabilities. The development of both signal processing hardware and software was also the scope of BAASP'2019.

This Conference was supported by the European Regional Development Fund Project No. 1.1.1.5/18/I/009 "Support to Ventspils University of Applied Sciences in Preparation of International Cooperation Projects for Research and Innovation" and No. 1.1.1.5/18/A/019 "Further Development of VIRAC Institutional and Scientific Capacity".

Dr.sc.ing. Romass Pauliks,
Chairman of the Scientific and Local Committee of BAASP'2019

sciendo

LATVIAN JOURNAL OF PHYSICS
AND TECHNICAL SCIENCES
2020, N 1-2

DOI: 10.2478/lpts-2020-0001

ANTARR – ETNA LOW FREQUENCY ANTENNA ARRAY

G. Tuccari*, M. Wunderlich, S. Dornbusch, G. G. Tuccari

INAF – Institute of Radioastronomy, 101 Gobetti Str., 40126 Bologna, ITALY
Max Planck Institute for Radio Astronomy,
69 Auf dem Hugel, 53121Bonn, GERMANY
HAT-Lab Ltd., 97 Milano Str., 95127 Catania, ITALY
*e-mail: tuccari@mpifr-bonn.mpg.de

A project called AntArr as a new application of the DBBC3 (Digital Base Band Converter, 3rd generation) is under development. A group of antennas operating at low frequency, in the range from 10 MHz up to 1500 MHz, are phased up for VLBI, pulsar and more recently for FRB observations. Part of the scientific programme is also dedicated to SETI activities in piggy-back mode. Dedicated elements can even be added to reach still lower frequencies to observe the range down to kHz frequencies. The DBBC3 manages the array operations in a selected portion of the band and the main characteristic is to synthesize a beam with an innovative approach. The final product of the array is a single station standard VLBI data stream for correlation with other antennas, or a synthesized beam for single dish observations. A number of antennas and array prototypes are under test at a location on the Etna volcano slope, with the aim to form a complete radio telescope of up to 1024 elements in 2020 and beyond. This project completes the lower part of the frequency spectrum covered in VLBI by the BRAND EVN project. The project AntArr is hosted and financed by HAT-Lab Ltd., which is the manufacturer of the DBBC family backends.

Keywords: *Antenna array, BRAND EVN, DBBC backend, VLBI*

1. INTRODUCTION

A project called AntArr as a novel application of the DBBC3 [1], [2] (Digital Base Band Converter, 3rd generation) is presented in the study. It is development under construction on the Etna volcano slopes at low altitude (about 600 meters). A group of antennas operating at low frequencies, in the range from 10 MHz to 1500 MHz, are phased up for VLBI or pulsar observations. Moreover, dedicated elements can be added to reach still lower frequencies to observe the range down to kHz frequencies. The DBBC3 manages the array operations in a selected portion

of the band and the main characteristic is to synthesize a beam with an innovative approach. The final product of the array is a single station standard VLBI data stream for correlation with other antennas, or a synthesized beam for pulsar observations. A number of different antennas, receivers and array prototypes have been implemented since the 2014 and have been under test at two locations for measurements and evaluation. In the end, the most suitable architecture has been selected in terms of performance, dimensions and cost. Such selected configuration is then used to build the array in a sufficient number of elements to allow for the complete functionality.

The selection of the antenna type considered the possibility to have add-on elements to reduce a lower range of frequency the array can receive up to a lower limit of few KHz. Such additional elements are under development and a number of prototypes are under evaluation.

2. ARRAY ARCHITECTURE

The general architecture of the AntArr instrument is schematically indicated in Figs. 1, 2 and 3. Each green circular element represents a single antenna. Most of such antennas are organised in arms to form a matrix whose rows are subject to the progressive formation of the array signal that is finally forwarded to one of the inputs of the DBBC3. A maximum number of 32 inputs are available for a maximum number of 32 elements in a single arm, bringing the maximum number of elements of the array to 1024. The arms are disposed in E-W oriented rows, having any row in both ends allows operating as an independent array of 'level one'. Groups of rows are organised in a further 'level two' array, and finally the entire set of groups is organised as 'level three' of array, which is the final arrangement. This distinction is motivated by the fact that separated elements in the array matrix can be selected, making use of cross correlation of the combined received signals to simplify the array calibration.

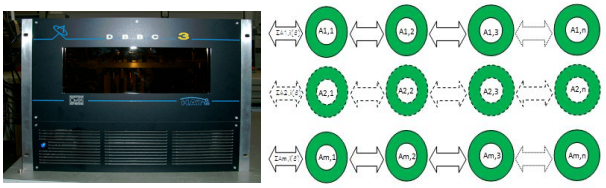

Fig. 1. Antenna array managed by the DBBC3.

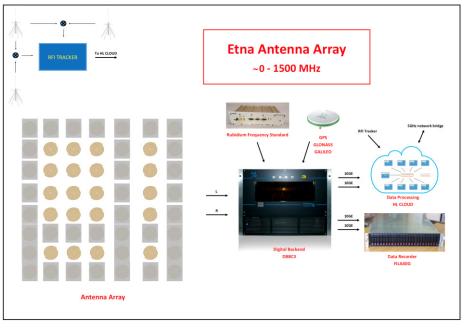

Fig. 2. Schematic structure of antenna array with its main components.

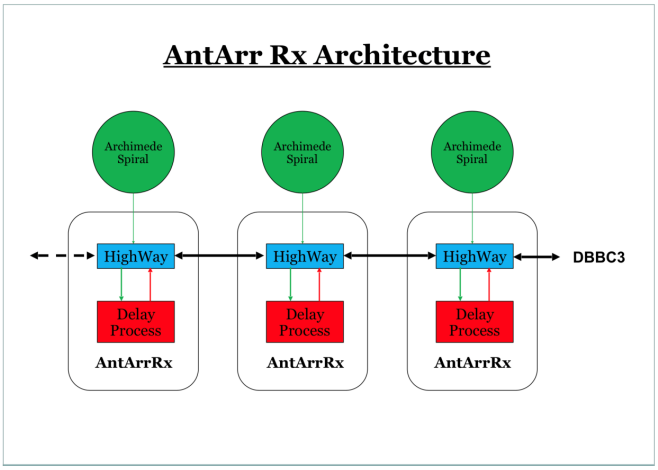

Fig. 3. Array signal distribution.

General features of the array and beam synthesis

The main general features of the instrument are as follows:

- Antenna prototype frequency range: 15 MHz–1500 MHz;
- Max. number of antennas in a single arm: 32;
- Max. number of arms with a single DBBC3: 32;
- Max. observation bandwidth of each arm: 1500 MHz;
- Analogue delay compensation digitally controlled at every antenna;
- Analogue summation for each arm at every antenna;
- Digital correlation between elements of the array;
- Digital correlation between elements of the array and the synthesized beam.

3. ANTENNAS AND RECEIVER

The signals of the developed antenna array are processed by the VLBI backend DBBC3L [3]. As mentioned above, a set of antennas is organised in arms, in groups managed by a single ADB3L-CORE3H in order to create one or more synthesized beams. The signal from each antenna has the model delay applied to compensate the path length difference of the incoming radiation relative to its direct neighbour antenna. The delayed signal is summed to this next neighbour.

The resulting signal has again the model delay applied relative to its next neighbour and the combined signal is added to it and so on, up to the DBBC3 processor. Any single beam is also available to be correlated with either the synthesized beam or with any other element in the array to precisely determine the delay residual with respect to the model of single elements as a function of the time. The signal of the source is then tracked with a mix of theoretical geometric model and the residuals determined with the array itself.

Figures 4a and 4b show the prototype of the selected antenna in double and single circular polarization, respectively, while its 3D beam is reported in Fig. 5.

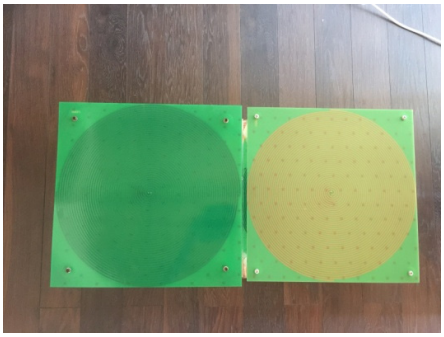

Fig. 4a. Antenna in double polarization.

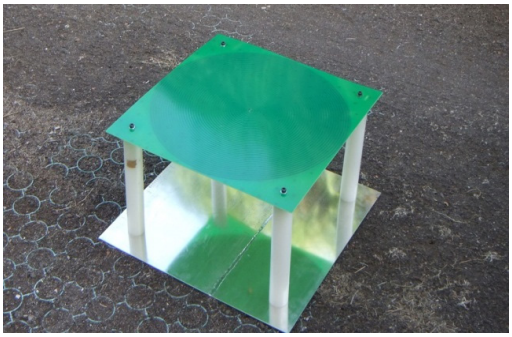

Fig. 4b. Antenna in single polarization.

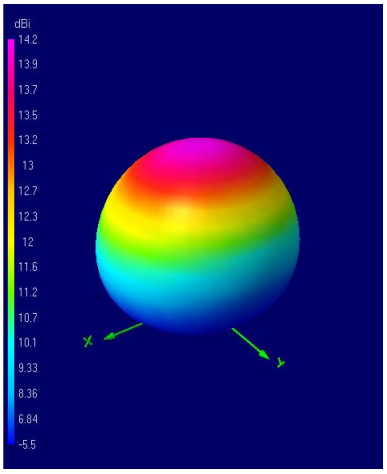

Fig. 5. Single antenna beam.

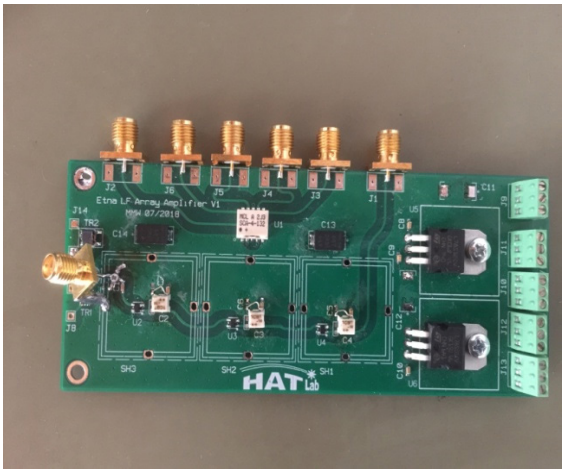

Fig. 6. The receiver, three amplification stages.

The receiver (Fig. 6) is a low-noise amplifier of three amplification stages with a high dynamic range. The receiver is composed of two boards, one for the amplification stages and the other for the delay control. The latter is included in the distribution cables and is controlled by the DBBC3. The entire single receiver with the antenna enclosure behaves at a system temperature in the order of 300 K at 500 MHz.

Particular care is to be applied for the implicit RFI crowded environment the array is asked to work in. Figures 7a and 7b show the RFI condition in the site where the array is under construction, the monitors for pointing and total power detected. Even in a severe environment portions of band can be selected where observations are still possible. In order to take into account this aspect, three wide range antennas looking at the terrestrial emissions have been dedicated to track and identify the direction of the worst case emissions: such information is considered in the beam forming so to make minimum contribution of side lobs of the synthesized beam. Dedicated software entirely developed by HAT-Lab research merges pointing beam forming and RFI minimisation. Then a two-way tracking is implemented, one

pointing to the extra-terrestrial source to be observed, and the other to the counter-pointing on the terrestrial emissions. This method is still under study and until now could provide attenuation of the RFI in the total power regime of up to 25–30 dB, resulting in a promising method when optimised.

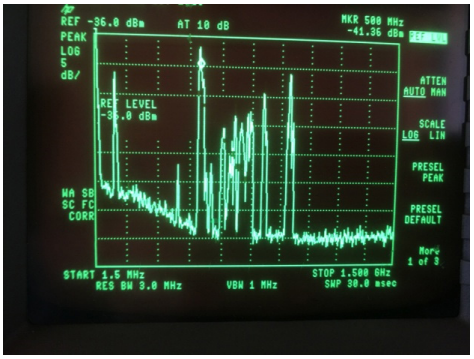

Fig. 7a. RFI environment in the Etna site.

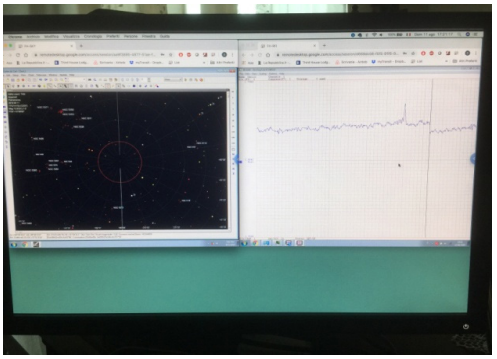

Fig. 7b. Monitors: array pointing, total power.

4. STATIONS AND ARRAY CHARACTERISATION

At the early stages of the project development, two stations have been equipped with a few prototypes for testing the network capability: one in the vicinity of the Noto radio telescope, the other on the northern slope of the Etna volcano at low altitude, the site where now the array will be fully installed. Figures 8a and 8b show a view of the relative position of the sites in Italy, in the Sicily Island, and one of the prototypes close to the Noto radio telescope.

Fig. 8a. Baseline Noto – Etna site.

Fig. 8b. Antenna prototype at the Noto radio telescope.

A drone equipped with a multi-frequency transmitter is used to test and characterise a single antenna and groups of antennas in the far-field regime. The vehicle can be placed in the sky at fixed positions controlled by an on-board GPS and an altimeter in order to determine the 3D complex beam of a single antenna and the part of the array under analysis. This method allows performing holographic measurements of the physical position of the single array element to make a map for the beam synthesis. Figure 9 illustrates the calibration method.

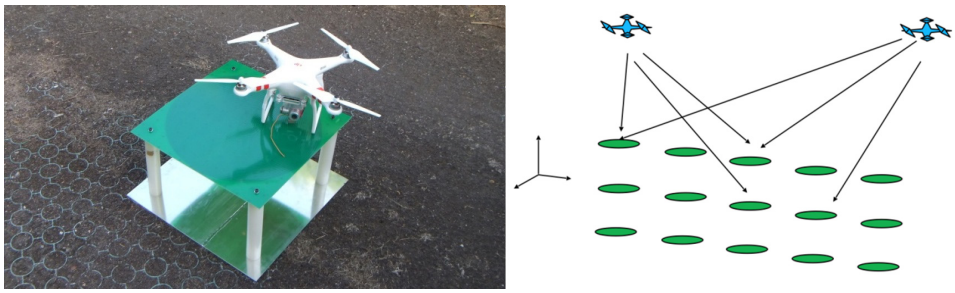

Fig. 11. Drone with a transmitter for 327, 654, 981 MHz is used for the array calibration.

5. CONCLUSIONS

The new antenna array named AntArr operating with a synthesis beam is under construction on the Etna volcano and mainly dedicated to VLBI observations. The array is an innovative demonstration prototype expected to operate in a low frequency range, starting at around 10 MHz and extending up to 1.5 GHz. Such frequency is a lower boundary of the BRAND EVN receiver, which is a project under development, financed under Radionet4 Horizon2020 and expected to cover the range between 1.5–15.5 GHz. Thus, the AntArr project is virtually extending a lower portion of the frequency spectrum for VLBI observations. The project is fully financed by HAT-Lab Ltd., the Italian company producing the DBBC VLBI backend family.

REFERENCES

1. Tuccari, G. (2011). DBBC3. In *Proceedings of the 20th EVGA Meeting and 12th Analysis Workshop* (pp. 19–21), Bonn, Germany.
2. Tuccari, G., Alef, W., Buttaccio, S., Tornatore, V., & Wunderlich, M. (2014). DBBC3: AntArr Project. In *Proceedings of Science, 12th European VLBI Network Symposium and User Meeting*, 7–10 October 2014, Cagliari, Italy.
3. Tuccari, G., Alef, W., Bertarini, A., Buttaccio, S., Casey, S., Comoretto, G., … & Wunderlich, M. (2014). DBBC3: VLBI at 32 Gbits per second. In *Proceedings of Science, 12th European VLBI Network Symposium and User Meeting*, 7–10 October 2014, Cagliari, Italy.

ANTARR – ETNAS ZEMFREKVENCES ANTENU MASĪVS

G. Tukari, M. Vunderlihs, S. Dornbušs, G. G. Tukari

K o p s a v i l k u m s

Projekts ar nosaukumu “AntArr” tiek izstrādāts kā jauna lietojumprogramma DBBC3 (3. paaudzes ciparu bāzes joslas pārveidotājs). Antenu grupa, kas darbojas zemo frekvenču diapazonā no 10 MHz līdz 1500 MHz, tiek pakāpeniski salāgota it īpaši lielas bāzes interferometrijas (VLBI), pulsāriem un nesen ātro radio uzliesmojumu (FRB) novērojumiem. Daļa no zinātniskās programmas veltīta arī SETI aktivitātēm. Antenas masīvam var pat pievienot klāt specializētus elementus, lai sasniegtu vēl zemākas frekvences un novērotu diapazonu līdz kHz frekvencēm. DBBC3 pārvalda antenu masīva operācijas izvēlētā joslas daļā, un galvenais uzdevums ir sintezēt staru ar inovatīvu pieeju. Antenu masīva gala produkts ir vienas stacijas datu straume VLBI standarta korelācijai ar citām antenām vai sintezēts stars novērojumiem vienas antenas režīmā. Vairāki antenas un bloku prototipi ir realizēti, un tie tiek pārbaudīti Etnas vulkāna nogāzes vietā ar mērķi 2020. gadā sāk veidot strādājošo radioteleskopu, kas sastāvēs no līdz pat 1024 elementiem. Šis projekts nosedz frekvenču spektra apakšējo daļu VLBI vajadzībām un ar to papildina BRAND EVN projektu. Projektu AntArr vada un finansē SIA “HAT-Lab”, kas ir DBBC saimes aparatūras ražotājs.

Atslēgas vārdi: *VLBI, DBBC ciparotājs, antenu masīvs, BRAND EVN*

sciendo

LATVIAN JOURNAL OF PHYSICS
AND TECHNICAL SCIENCES
2020, N 1-2

DOI: 10.2478/lpts-2020-0002

MODELLING OF SIPM PERFORMANCE FOR DETECTION OF CHERENKOV RADIATION FROM EXTENSIVE AIR SHOWERS IN UV AND VISIBLE RANGES FOR APPLICATION AT THE TAIGA-IACT TELESCOPE

A.A. Bogdanov*, E.E. Kholupenko,
Yu.V. Tuboltsev, Yu.V. Chichagov

Ioffe Institute, 26 Politekhnicheskaya Str., 194021, St. Petersburg, RUSSIA
*e-mail: Alexander.A.Bogdanov@mail.ioffe.ru

A novel cluster of sensitive detectors based on silicon photomultipliers (SiPM) is being developed for the Cherenkov gamma-ray telescope TAIGA-IACT (Tunka valley, Republic of Buryatia, Russia). The cluster will be able to detect Cherenkov radiation from extensive air showers in two wide bands: 250–300 nm (UV) and 250–700 nm (visible and UV). Each pixel consists of a Winston cone, 4 SiPMs with the total sensitive area of 144 mm^2, and readout electronics based on fast analogue memory. During operation in the UV band, a UV-bandpass filter is used to suppress cluster sensitivity in the visible range. In order to evaluate the detection efficiency of the selected SiPMs, a specific software simulator of SiPM output signal has been developed. This simulator takes into account such inherent parameters of SiPMs as total number of microcells, their recharge time, the dark count rate, the effective detection area, the quantum efficiency, the crosstalk between microcells, as well as conditions of SiPM operation, namely, the background noise and the Ohmic load in the readout (front-end) electronics. With this simulator it is possible to determine the expected trigger threshold under given conditions and parameters of selected detectors. Based on preliminary simulations, OnSemi MicroFJ-60035 SiPM chips have been chosen for the novel cluster of TAIGA-IACT. These SiPMs have sensible efficiency in the ultraviolet range (5–20% in the 250–300 nm band) and are distinguished by the presence of a fast output, which allows one to capture a low amplitude signal above a relatively high background noise.

Keywords*: Extensive air shower, IACT, photomultipliers, SiPM*

1. INTRODUCTION

Gamma-ray astronomy is an important field of observational astrophysics. It allows one to investigate the most energetic events in the Galaxy and beyond, such as explosions at late stages of stellar evolution [1], stellar mergers, propagation of interstellar shock waves, and intense high-velocity outflows (jets) formed in the

vicinity of super massive black holes in active galactic nuclei [2]. Modern methods for observing high energy cosmic gamma-quanta cover the range up to ~100 TeV [3], [4] and even beyond [5].

Cherenkov gamma-ray telescopes and their arrays – Cherenkov gamma-ray observatories – are the most sensitive instruments suited for observations of cosmic gamma-rays in the 10 GeV – 100 TeV range because of their effective area (about 10^4–10^6 m^2). Rather than registering the primary gamma-quantum, they detect Cherenkov radiation generated by high-energy electrons and positrons of extensive air showers (EASs) induced by the primary gamma-quantum during its interaction with the Earth's atmosphere. The Cherenkov radiation from an EAS is emitted within a narrow cone in the motion direction of the primary particle and illuminates an area with diameter of 200–500 m (depending on primary particle energy [4], [6]) on the Earth's surface.

At major modern imaging atmospheric Cherenkov telescopes (IACTs) and observatories (MAGIC, VERITAS, H.E.S.S.), measurements of Cherenkov light flashes are performed using cameras based on high-voltage vacuum photomultiplier tubes (PMTs). This leads to significant restrictions of available exposure because Moon illumination and atmosphere illumination during twilight may cause full blinding or even fatal damage of these PMTs. In this regard, it is likely that semiconductor avalanche photodetectors – silicon photomultipliers (SiPM) – will be used in the detector blocks of the foreseen telescopes of the new (fourth) generation (for example, CTA and ALEGRO [7]). At present, employment of SiPM-based camera at FACT telescope already allows one to perform observations even during moonlit nights [8], and it significantly enlarges exposures of cosmic gamma-ray sources. An additional almost equally efficient method to increase the duty cycle is the use of UV-pass filters blocking optical emission (e.g., [9], [10]). This approach leads to strong suppression of the noise in the telescope camera induced by the night sky background and Moon illumination and conservation of a significant part of the EAS Cherenkov signal, as its spectrum peaks at 300–330 nm.

Currently, a novel cluster of 28 sensitive SiPM detectors with replaceable UV filters is being developed for the Cherenkov gamma-ray telescope TAIGA-IACT (Tunka valley, Republic of Buryatia, Russia) in order to probe both mentioned techniques of duty cycle extension and to improve the gamma-hadron separation. Such techniques are likely to be employed at larger-scale Cherenkov observatories (e.g., ALEGRO [7]). Within the next 2–3 years, it is planned to replace one of 20 PMT-based detecting clusters of one TAIGA-IACT unit [4] by a new cluster based on OnSemi MicroFJ-60035 SiPMs (further on –"MicroFJ"). In the frame of this project, numerical modelling of the TAIGA-IACT telescope unit and, in particular, modelling of the new detecting cluster are required. Such modelling includes development of a MicroFJ pixel simulator, which is the subject of the present paper.

2. PARAMETERS OF CHERENKOV FLASH SIGNALS TO BE REGISTERED WITH TAIGA-IACT

A flash of 260–700 nm Cherenkov light produced by an EAS and later focused by a mirror of an IACT is short (about 10–15 ns) and weak (the integral fluxes

registered by modern Cherenkov telescopes are ~3–3·10^4 photon/m^2). The leading edge of such a signal is about 2–3 ns long (depending on the primary particle type). At distances r < 120 m from the EAS axis, over 90 % of Cherenkov photons will come within a 10 ns interval. The TAIGA-IACT telescope has the mirror area of about 10 m^2, a 10° field of view (FoV) [4], the camera pixel area of about 9.5 cm^2. With an account of the telescope optical transmission coefficients and the photon detection efficiency (PDE) of present detectors, this leads to ~1 TeV energy threshold of this instrument. Preliminary modelling of TAIGA-IACT shows that Cherenkov radiation from EAS induced by a cosmic gamma-quantum with energy 1 TeV would yield a signal of about 13 photoelectrons (p.e.) per detector pixel for a 10 ns frame (hereafter 1 p.e. means the signal from 1 triggered SiPM detector microcell, i.e., 1 electron avalanche, since microcells operate in the Geiger mode). Note that the signal in individual brightest pixels can be 3–7 times higher than the indicated average value and may reach ~10^2 p.e./frame.

Since the signal from an EAS is generated by the Cherenkov radiation, its spectrum (illustrated in Fig. 1) is described by the Frank-Tamm law averaged over ensembles of ultra-relativistic electrons and positrons of EAS moving with energies larger than the critical value (~21 MeV near the Earth surface), with a cutoff below ~300 nm, which is due to absorption of photons by atmospheric ozone.

The level of night sky background depends on locality (defined by the latitude and longitude), climate, and day time. The typical background level for the Tunka valley on a moonless night is about 3·10^{12} photon·m^{-2}·s^{-1}·sr^{-1} in the 300–600 nm band. For the TAIGA-IACT telescope, the modelled noise from background photons would amount to (2.5 ± 0.8) p.e. in a 10 ns frame. A typical spectrum of night sky background is shown in Fig. 1 (based on data from [11]).

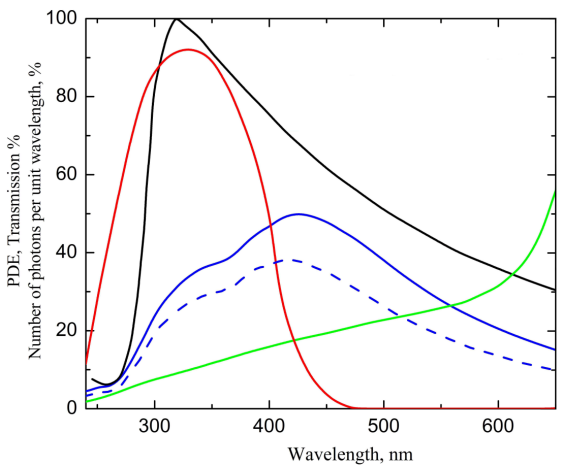

Fig. 1. Model spectra of source signal and sky background along with typical wide UV filter transmission and detector efficiency: black – a typical Cherenkov flash spectrum, green – night sky background spectrum; blue – the PDE of OnSemi MicroFJ60035 at 6 V (solid) and 2.5 V (dashed) overvoltage; red – a commercial Subei/ZWB3 wide UV filter [9] transmission curve.

As the foreseen operation range of TAIGA-IACT telescope with an upgraded camera is 1–100 TeV, with an account of the modelled background and EAS signal

strength, one may expect that the signal from one camera pixel consisting of 4 SiPM detectors would not exceed 10^4 p.e. for a 10 ns frame. It is quite acceptable because the number of microcells in such a pixel would be about $9 \cdot 10^4$. The signal range of 1–10^4 p.e. is a requirement for the front-end readout system currently developed at the Ioffe Institute.

3. MODELLING OF DETECTOR PERFORMANCE

The developed model of OnSemi MicroFJ-60035 SiPM [12] detector pixel accounts for photon registration within detector microcells, dark counts, crosstalk, background noise from the night sky, and formation of the output electric signal. For simplicity, the internal detector noise and the noise from readout chains are not taken into account. No broadening of the output signal due to these chains has been considered.

Detector modelling yields oscillograms of the output signal, which are based on the evolution of the number of triggered microcells (or photoelectrons, further – p.e.), as the amplitude of the whole SiPM signal is proportional to the number of avalanched microcells. As the capacity of the SiPM detector C_{DET} and the readout resistance R are significant, the signal amplitude decays with non-zero time constant (see Fig. 2).

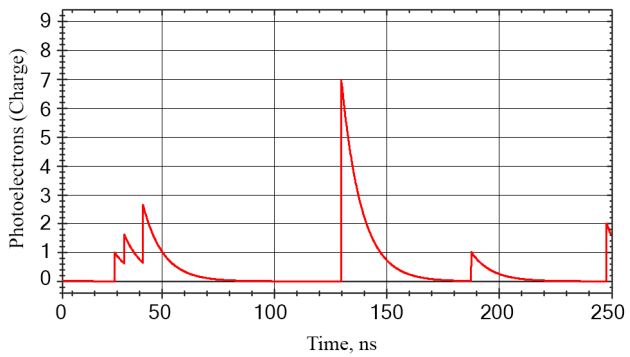

Fig. 2. A model detector oscillogram. The signal at 130 ns comes from source photons (6 p.e.) and a crosstalk event (1 p.e.).

For illustrative purposes, a toy-model 14×14 microcell detector is shown in Fig. 3, while the number of microcells in a real detector can reach several by ten thousand. We have modelled a SiPM-based detector consisting of 2×2 MicroFJ chips and amounting to 89 168 microcells.

Each of the green microcells in Fig. 3 corresponds to a source photon, which adds 1 p.e. to the summed amplitude of the model output signal. Each of the triggered microcells may also initiate an avalanche in one of the neighbouring cells (at an 8 % crosstalk probability for +2.5 V overvoltage [12]), which also adds 1 p.e. to the output.

Crosstalk is a significant mechanism affecting the output signal of SiPM detector. A simplified explanation of crosstalk is that an infrared (IR) photon may

be emitted in a microcell within the avalanche process triggered either by a source/background photon or by a dark current event. If such an IR photon is energetic enough, it can trigger an avalanche in one of the neighbouring microcells. Hence, the output amplitude of the detector becomes uncertain, and this uncertainty rises with the crosstalk probability [13].

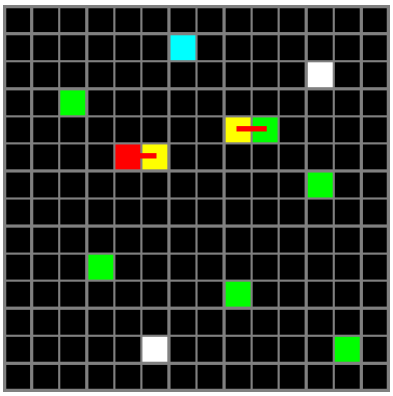

Fig. 3. A toy-model 14×14 microcell detector pixel with various types of events shown: source (green), crosstalk (yellow), hit twice within the relaxation time (red), sky background (white), dark counts (cyan). The red bars indicate the crosstalk direction.

The crosstalk simulation algorithm is as follows. Once a microcell is triggered, one of the neighbouring microcells will also be triggered with a certain probability (e.g., 8 %) and according to the "4 nearest neighbours" model [13]. Moreover, a chain of crosstalk triggered microcells may be formed because they can also cause IR-photons. In practice, such chains are rarely larger than 2 or 3 microcells. We do not consider here the delayed crosstalk [14] and the afterpulsing activity of the MicroFJ detector.

Crosstalk-induced microcells are shown in yellow (Fig. 3), and the crosstalk direction is shown with a red bar. After a microcell is triggered either by a source or background photon, or by crosstalk, or dark count event, its input to the summed detector signal evolves according to discharge of the corresponding RC contour, i.e., the signal decays ~ $\exp(t/R\,C_{\mathrm{DET}})$, where t is time, R is the load resistance.

4. DETECTOR BACKGROUND AND DARK COUNT RATE

The dark count rate of silicon photomultipliers is much higher than that of traditional vacuum photomultipliers. Together with the background photons they decrease the signal-to-noise ratio. At +2.5 V overvoltage, the dark count rate of MicroFJ SiPM detectors is about 50 kHz/mm^2; hence, for a 2×2 MicroFJ SiPM pixel proposed for the camera of TAIGA-IACT it would yield the rate ~7 MHz/pixel. Such a rate is not significant for observations in the visual band, where the dark sky background is about ~250 MHz/pixel (~2.5 p.e. for a 10 ns frame), but in the 250–300 nm band it becomes an important issue, as the dark sky background in the ultraviolet range is substantially lower (< 1 MHz/pixel).

It should be noted that reading out from the fast output of MicroFJ SiPM (RC constant ~3 ns) would allow us to avoid charge accumulation even for the relatively high sky background expected in the visual band; hence, individual pulses are not likely to overlay and saturate the output.

5. MICROCELL RELAXATION AND DETECTOR SATURATION

A triggered microcell cannot produce an avalanche signal until it is recharged. The characteristic recharge time constant for MicroFJ is about 50 ns [12]. As the number of microcells in a SiPM detector is large and the expected background is relatively low, the simulation software marks the triggered microcells (red in Fig. 3) if a photon hits it during the full recharge time (about 150 ns), but does not enhance the modelled output signal. In practice, there is a small chance that a microcell that has not fully recharged still produces an avalanche.

For the TAIGA-IACT camera, the expected background photon rate in an optical pixel containing 4 MicroFJ SiPM detectors is about 250 MHz, and the dark count rate is about 7 MHz. As the total number of microcells in such a pixel equals 89 168, the probability of a photon hitting a microcell during its recharge is about 0.05 %. The expected number of optical range photons from an EAS is about 150; hence, the probability of such a photon to hit a recharging microcell in a 10 ns frame is about 18 %, which would lead to < 1 % uncertainty of the EAS signal.

We have modelled detector saturation at maximal foreseen photon loads (about 10^4 photons in a 10 ns frame). Such a photon signal would trigger on average (11.5 ± 0.1) % of the total 89 168 microcells. The output signal appeared only about 2 % higher than 10^4 p.e. because about 6 % of the incoming photons and crosstalk events overlapped with the already triggered microcells. Hence, we concluded that the detector would keep linear and would not saturate at the modelled loads.

6. EVALUATION BOARD FOR A MICROFJ-BASED DETECTOR

We have fabricated and investigated a simple evaluation board for a MicroFJ-based detector (Fig. 4). The input stage consists of a current follower on a BFT93 transistor and a voltage amplifier on a wideband low-noise operational amplifier AD8099. This input stage provided amplification and conversion of detector current from the fast output with transimpedance 1600 Ω in a bandwidth of more than 200 MHz.

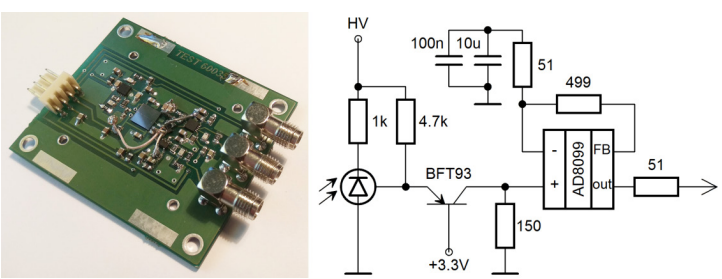

Fig. 4. An evaluation board for a MicroFJ-based detector pixel produced by the authors.

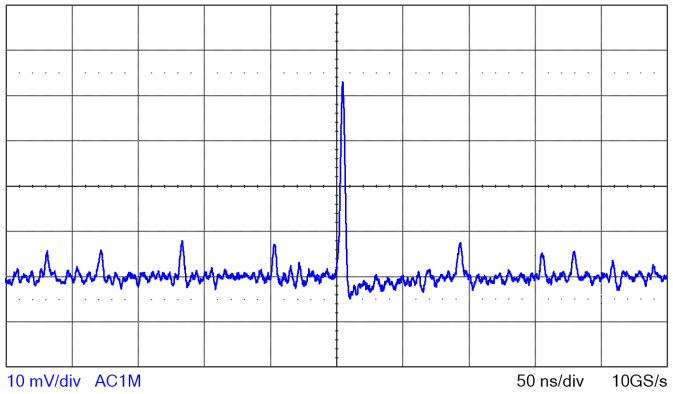

Fig. 5. Dark count signal measured from SiPM detector OnSemi MicroFJ-60035 at +2.5 V overvoltage. The widths of the leading and trailing edges were about 3 ns. The vertical box scale is 10 mV; the horizontal scale is 50 ns.

Experiments in a dark volume have shown that the widths of the leading and trailing edges are about 3 ns. A dark current impulse on top of multiple crosstalk events observed with frequency ~1 Hz is shown in Fig. 5. The amount of crosstalk in such peaks can be approximately estimated from this frequency and known crosstalk probability (8 %) as 7 p.e. (1 microcell triggered by dark current and 6 crosstalk events).

7. CONCLUSIONS

We have modelled parameters of output signals from a Cherenkov telescope pixel made of 4 SiPM MicroFJ detectors for realistic photon loads. The modelling accounted for microcell crosstalk, dark counts, sky background and source parameters, as well as for some parameters of readout electronics. Based on this modelling, we may conclude that such SiPM-based pixels can be employed for future upgrade of the TAIGA-IACT camera and proceed to optimisation of the camera front-end readout scheme.

ACKNOWLEDGEMENTS

The research has been supported by RSF grant 19-72-20045.

REFERENCES

1. Brazier, K.T.S., Carraminana, A., Chadwick, P.M., Dipper, N.A., Lincoln, E.W., McComb, T.J.L., … & Turver, K.E. (1990). SN1987a – Updated Limit to 400 GeV Gamma Ray Emission Using the Narrabri VHE Gamma Ray Telescope – May 1989. *Nucl. Phys. B. Proc. Suppl., 14* (1), 188−190.
2. Ahnen, M.L., Ansoldi, S., Antonelli, A., Antoranz, P., Babić, A. Banerjee, B., … & Zottmann, N. (2015). Very High Energy γ-Rays from the Universe's Middle Age: Detection of the z = 0.940 Blazar PKS 1441+25 with MAGIC. *The Astrophysical Journal Letters, 815* (2), L23−L31.

3. Aharonian, F., Akhperjanian, A., Beilicke, M., Bernlöhr, K., Börst, H.-G., Bojahr, H., … & Wittek, W. (2004). The Crab Nebula and Pulsar between 500 GeV and 80 TeV: Observations with the HEGRA Stereoscopic Air Cerenkov Telescopes. *The Astrophysical Journal, 614* (2), 897−913.
4. Kuzmichev, L.A., Astapov, I.I., Bezyazeekov, P.A., Boreyko, V., Borodin, A.N., Budnev, B.M., … & Yashin, I.I. (2018). TAIGA Gamma Observatory: Status and Prospects. *Physics of Atomic Nuclei, 81* (4), 497−507.
5. Amenomori, M., Bao, Y.W., Bi, X.J., Chen, D., Chen, T.L., Chen, W.Y., … & Zhou, X.X. (2019). First Detection of Photons with Energy Beyond 100 TeV from an Astrophysical Source. *eprint arXiv:*1906.05521.
6. Mishev, A., Mavrodiev, S., & Stamenov J. (2005). Gamma Rays Studies Based on Atmospheric Cherenkov Technique at High Mountain Altitude. *International Journal of Modern Physics A, 20* (29), 7016–7019.
7. Bykov, A. M., Aharonian, F. A., Krassilchtchikov, A. M., Kholupenko, E.E., Aruev, P.N., Baiko, D.A., … & Chicagov, Yu.V. (2017). Cherenkov Gamma-Ray Telescopes: Past, Present, Future. ALEGRO Project. *Technical Physics, 62* (6), 819–836.
8. Knoetig, M. L., Biland, A., Bretz, T., Buß, J., Dorner, D., Einecke, S., … & Zanglein, M. (2013). FACT – Long-term Stability and Observations during Strong Moon Light. In *Proc. of the 33rd ICRC, Rio de Janeiro,* id. 695, arXiv:1307.6116.
9. Guberman, D., Cortina, J., Garcia, R., Herrera, J., Manganaro, M., Moralejo, A., … & Will, M. (2015). Using UV-pass Filters for Bright Moon Observations with MAGIC. In *Proc. of the 34th International Cosmic Ray Conference (ICRC2015)*, 34, id. 1237, arXiv:1509.02048.
10. Kholupenko, E.E., Bykov, A.M., Aharonyan, F.A., Vasiliev, G.I., Krassilchtchikov, A.M., Aruev, P.N., … & Nikolaev, A.V. (2018). Detection of UV Radiation from Extensive Air Showers: Prospects for Cherenkov Gamma-Ray Astronomy. *Technical Physics*, *63* (11), 1603–1614.
11. Leinert, Ch., Bowyer, S., Haikala, L.K., Hanner, M.S., Hauser, M.G., Levasseur-Regourd, A.-Ch., … & Witt, A.N. (1998). The 1997 Reference of Diffuse Night Sky Brightness. *Astronomy and AstrophysicsSupplement, 127*, 1–99.
12. Semiconductor Components Industries. (2018). OnSemi J-Series SiPM Sensors Datasheet. Rev. 6, MICROJ−SERIES/D. Available at https://www.onsemi.com/pub/Collateral/MICROJ-SERIES-D.PDF
13. Gallego, L., Rosado, J., Blanco, F., & Arqueros F. (2013). Modeling Crosstalk in Silicon Photomultipliers. *JINST*8 P05010. http://dx.doi.org/10.1088/1748-0221/8/05/P05010
14. Nagy, F., Mazzillo, M., Rennet, L., Valvo, G., Sanfilippo, D., Carbone, B., … & Molnar, J. (2014). Afterpulse and Delayed Crosstalk Analysis on a STMicroelectronics Silicon Photomultiplier. *Nuclear Instruments and Methods in Physics Research Section A* 759, 44–49.

SIPM VEIKUMA MODELĒŠANA ČERENKOVA STAROJUMA NOTEIKŠANAI NO PLAŠĀM GAISA LIETUSGĀZĒM UV STARU UN REDZAMĀ DIAPAZONĀ PIELIETOŠANAI TAIGA-IACT TELESKOPĀ

A.A. Bogdanovs, E.E. Kholupenko, Yu.V. Tubolcevs,
Yu.V. Čičagovs

K o p s a v i l k u m s

Čerenkova gamma staru teleskopam TAIGA-IACT (Tunkas ieleja, Burjatijas Republika, Krievija) tiek izstrādāts jauns jutīgu detektoru klasteris, kura pamatā ir silīcija fotopavairotāji (SiPM). Klasteris spēs noteikt Čerenkova starojumu no plašām gaisa lietusgāzēm divās platjoslās: 250–300 nm (UV) un 250–700 nm (redzamā un UV staru diapazonā). Katru pikseli veido Vinstona konuss, 4 silīcija fotopavairotāji ar kopējo jutīguma laukumu 144 mm^2 un nolasīšanas elektroniku, kuras pamatā ir ātra analogā atmiņa. Darbības laikā UV joslā tiek izmantots UV joslas caurlaidības filtrs, lai nomāktu klastera jutīgumu redzamā diapazonā. Lai novērtētu izvēlēto SiPM noteikšanas efektivitāti, ir izstrādāts īpašs programmatūras simulators SiPM izejas signālam. Šis simulators ņem vērā tādus SiPM raksturīgos parametrus kā kopējo mikrošūnu skaitu, to uzlādes laiku, tumšo skaitīšanas ātrumu, efektīvo noteikšanas laukumu, kvantu efektivitāti, šķērsrunu starp mikrošūnām, kā arī SiPM darbības apstākļus, proti, fona troksni un omu slodzi nolasīšanas (priekšgala) elektronikā. Ar šo simulatoru ir iespējams noteikt paredzamo sprūda slieksni, ņemot vērā noteiktus apstākļus un izvēlēto detektoru parametrus. Par pamatu ņemot provizoriskās simulācijas, jaunajam TAIGA-IACT klasterim ir izvēlētas OnSemi MicroFJ-60035 SiPM mikroshēmas. Šiem SiPM ir saprātīga efektivitāte ultravioletā starojuma diapazonā (5–20% diapazonā no 250 līdz 300 nm), un tos atšķir ar ātru izeju, kas ļauj uztvert zemas amplitūdas signālu virs relatīvi augsta fona trokšņa.

Atslēgas vārdi: *IACT, fotopavairotāji, plaša gaisa lietusgāze, SiPM*

sciendo

LATVIAN JOURNAL OF PHYSICS
AND TECHNICAL SCIENCES
2020, N 1-2

DOI: 10.2478/lpts-2020-0003

3-WAY LUNAR RADIO RANGING EXPERIMENT ON RT-32 RADIO TELESCOPES

D. Marshalov[1]*, J. Ping[2], W. Li[2], M. Wang[2], J. Sun[2],
Yu. Bondarenko[1], M. Vasilyev[1], E. Yagudina[1]

[1] Institute of Applied Astronomy, Russian Academy of Sciences,
10 Nab. Kutuzova, 191187, St.Petersburg, RUSSIA
[2] National Astronomical Observatories, Chinese Academy of Sciences,
20A Datun Road, 100012, Beijing, CHINA
*e-mail: marshalov@iaaras.ru

Since 2017, the Institute of Applied Astronomy of the Russian Academy of Sciences in cooperation with the National Astronomical Observatories of the Chinese Academy of Sciences has been conducting observations of the Chang'E-3 lander carrier wave signal. The paper presents the features of observation scheduling and results of data processing. High-precision phase radar measurements have been obtained with an instrumental error of 1–2 mm. The deviation of residuals in model calculations does not exceed ± 1 cm. The estimates of CE-3 lander position have been obtained with an accuracy of 0.5", 7.4 m and 3.2 m in celenocentric cylindrical longitude, Px and Py coordinates, respectively.

Keywords: *Chang'E-3, digital phase lock loop, lunar ephemeris, lunar radio ranging, phase measurement, radio telescope*

1. INTRODUCTION

In December 2013, the Chinese spacecraft Chang'E-3 (CE-3) landed on the surface of the Moon [1]. The lander was equipped with the transceiver device (transponder) operating in the X-band. The transponder was designed to receive a 7.2 GHz signal and its coherent reradiation at a frequency of 8.47 GHz.

Radio telescopes at Jiamusi and Kashi stations of the Chinese Deep Space Network with 66 m and 35 m antennas [2] regulary transmit the signal to CE-3. Reradiated signal from the transponder is recorded simultaneously by the 32 m radio telescopes (RT-32) at Svetloe, Zelenchukskaya and Badary observatories [3], as well as by the radio telescopes at the Seshan, Kunming and Urumqi observatories that are part of the National Astronomical Observatories of the Chinese Academy of Sciences

(NAOC). Thus, the Lunar Radio Ranging (LRR) technique was implemented, which allowed estimating the lander position and the model parameters of the orbital and rotational motion of the Moon regardless of lunar laser ranging (LLR) observations [4]. Expected impact of the LRR observations on the lunar ephemeris accuracy was estimated using numerical simulation [5].

Compared with the LLR, LRR has several advantages such as independence of weather conditions and the phase of the Moon, reduced requirements for target tracking accuracy, simultaneous observation by several stations and a larger number of stations that can record a signal. Simultaneous reception of a transponder signal by two or more radio telescopes is called 3-way LRR, reducing the uncertainty in lander position, but increasing the number of estimated parameters. In the following sections, we present the description of the methods used and the results of LRR experiments.

2. OBSERVATIONS AND DATA PROCESSING

A software complex was developed for scheduling LRR observations. It determined joint observation windows and formed an ephemeris file for a specified configuration of the transmitting and receiving antenna systems and selected near-Earth object (asteroid, comet or spacecraft). Planetary ephemeris DE430 [6] and corrections to the Earth's rotation parameters (the pole coordinates, the precession, the nutation, and the universal time) were used in the software complex to calculate the ephemeris files for the radio telescope control system.

Observations were carried out automatically on RT-32 according to a schedule in X-band [7]. A signal from CE-3 transponder with a frequency of 8.47 GHz was recorded, taking into account the Doppler shift. The radio telescope receiving system converted the signal from SHF to an intermediate frequency of 390 MHz. Then, the data acquisition system P1002M [8] converted the signal to video frequencies in the 2 MHz bandwidth from intermediate frequencies. The data were recorded by the Mark5B registration system with two-bit sampling. Then, the recorded data were transmitted for processing by the optical fibre channels.

Processing of observation data was divided into two stages. At the first stage of processing, the integrated observable phase φ of the recorded signal at a given time was calculated. Using the obtained phase φ, at the second stage, the selenocentric coordinates of the lander and phase ambiguities, corrections to time scales of the observatories, tropospheric and ionospheric delays were determined.

The digital phase-locked loop (DPLL) was used to calculate the integral phase φ of the recorded signal [9]. The implemented algorithm is shown in Fig. 1. The input signal was multiplied by the current value of the digital signal generator with the model phase φ_n. Then the resulting complex signal was accumulated over an update interval. Residual phase $\tilde{\varphi}_n$ for the given n-th interval was calculated as the complex sum U argument. Residual phase was passed to the loop filter to assist in the generation of model phase rate. The 3rd-order digital loop filter used residual phase values $\tilde{\varphi}_n$ to estimate phase rate $\dot{\varphi}_{n+1}$ for the $(n+1)$-th interval according to

$$\dot{\varphi}_{n+1}T = K_1\tilde{\varphi}_n + K_2\sum_{i=1}^{n}\tilde{\varphi}_i + K_3\sum_{i=1}^{n}\sum_{j=1}^{i}\tilde{\varphi}_j,$$

where $\dot{\varphi}_{n+1}T$ is phase change per update interval T=0.01 sec and loop coefficients K_1= 5.218E-2, K_2=1.210E-3, K_3=1.052E-5 for loop noise bandwidth of 2 Hz. Then these values were used to calculate the next model phase φ_n, while the observable phase φ was obtained from φ_n and phase residual $\tilde{\varphi}_n$ at a given time.

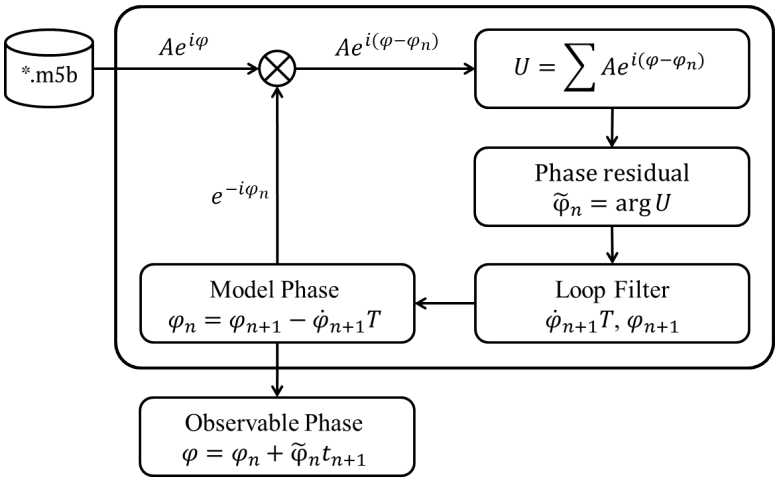

Fig. 1. Algorithm of the digital phase-locked loop for obtaining observable phase.

To compensate the influence of the atmosphere on the propagation of radio signals, we used tropospheric and ionospheric delays from IGS data. The tropospheric delay was calculated using Vienna mapping functions based on the weather data of each station. For this purpose, wet and hydrostatic delays at the zenith were determined. The zenith delay was projected onto the source-station line of sight using the mapping function [13]. The ionosphere was modelled by one thin layer at an altitude of 450 km above the Earth's surface. To calculate the ionospheric delay, the mapping function [12] was used.

Phase modelling used the following data and models:

- EPM-2014 [10] ephemeris to calculate geocentric position of the Moon and lunar rotation parameters;
- LRR and LLR observational models implemented in ERA system [11], which included all required IERS recommendations [12];
- for each radio telescope and observation interval, phase ambiguity, zenith wet delays and station clocks were adjusted.

As a result, the corrections to a priori values of the CE-3 lander coordinates were obtained. Parameters of the orbital and rotational motion of the Moon, radio telescope positions, as well as Earth orientation parameters were not estimated but fixed to their a priori values.

3. RESULTS

During the period from December 2017 to June 2018, six CE-3 3-way LRR observation sessions were successfully conducted. We also had 2-way LRR data obtained in 2014. Table 1 presents the dates of observations, configurations of receiving-transmitting stations and instrumental accuracy obtained for each observation session expressed in standard deviations (RMS) of the integral phase in mm.

Table 1

CE-3 Observations Obtained in 2014 and 2017/2018

Date	Configuration	Phase RMS, mm
2014-11-13	Jiamusi–Jiamusi	–
2014-12-03	Jiamusi–Jiamusi	–
2014-12-04	Jiamusi–Jiamusi	–
2014-12-05	Jiamusi–Jiamusi	–
2014-12-06	Jiamusi–Jiamusi	–
2014-12-07	Jiamusi–Jiamusi	–
2014-12-08	Jiamusi–Jiamusi	–
2014-12-09	Jiamusi–Jiamusi	–
2014-12-10	Jiamusi–Jiamusi	–
2017-12-07	Kashi–Svetloe	1.17
2017-12-10	Kashi–Svetloe	1.28
2018-03-31	Jiamusi–Badary	2.01
2018-04-02	Jiamusi–Badary	2.95
2018-06-25	Kashi–Badary	1.72
2018-06-27	Kashi–Badary	2.13

We obtained the selenocentric coordinates of the lander, tropospheric and ionospheric delays, and corrections to the time scales of the observatories. As a result, the deviation of phase residuals in model calculations did not exceed ±10.0 mm (see Fig. 2). The estimates of CE-3 lander position were obtained to be 19.532° W, 1245291.01 m and 1208076.4 m, with rms deviation 0.5”, 7.4 m and 3.2 m in selenocentric cylindrical longitude, P_x and P_y coordinates, respectively. Principal Axis (PA) coordinate system of EPM [10] ephemeris was used in this study.

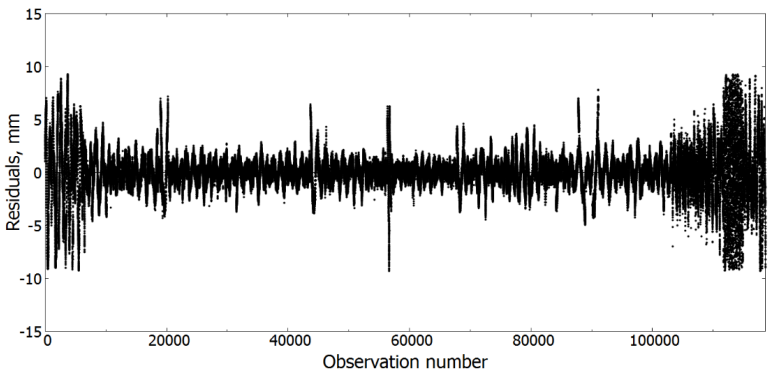

Fig. 2. Residuals of 2-way and 3-way LRR-observation.

4. CONCLUSIONS

The analysis of residuals of LRR observations confirmed high accuracy of the performed measurements. The standard deviation of phase LRR observations was 1–3 mm. LRR observation residuals obtained from the Kashi–Badary configuration did not exceed ±10.0 mm.

Using 2-way LRR observations carried out in 2014, the selenocentric PA coordinates of CE-3 lander were determined, the values of which were: X=1173627.868 m, Y= -416350.220 m and Z=1208076.399 m. A comparison with the results obtained from 3-way observations during 2017–2018 showed a good match.

ACKNOWLEDGEMENTS

The work of D. Marshalov and Yu. Bondarenko in terms of conducting and processing the phase radar observations has been supported by the Russian Science Foundation under grant No. 16-12-00071 and performed at the Institute of Applied Astronomy of the Russian Academy of Sciences.

REFERENCES

1. Li, C., Liu, J., Ren, X., Zuo, W., Tan, X., Wen W., … & Uuyang, Z. (2015). The Chang'e 3 Mission Overview. *Space Science Reviews, 190*, (1–4), 85–101.
2. Xu, D., Dong, G., Wang, G., Li, H., & Jiang, W. (2016). First Geodetic VLBI Sessions with the Chinese Deep Space Stations Jiamusi and Kashi. *Advances in Space Research*, *58*, 1638–1647.
3. Ivanov, D.V., Uratsuka, M.-R., Ipatov, A.V., Marshalov, D.A., Shuygina, N.V., Vasilyev, M.V., … & Suvorkin, V.V. (2018). Russian-Cuban Colocation Station for Radio Astronomical Observation and Monitoring of Near-Earth Space. *Astrophysical Bulletin*, *73* (2), 257–266.
4. Ping, J., Meng, Q., Wang, M., Tang, G., Jian, N., Wang, Z., … & Cao, J. (2014). First 3-Way Lunar Radio Phase Ranging and Doppler Experiment in Chang'E-3 Lander Mission. In *European Planetary Science Congress 2014, EPSC Abstracts, 9*, EPSC2014-226-1.
5. Vasilyev, M.V., Shuygina, N.V., & Yagudina, E.I. (2017). Expected impact of the Lunar Lander VLBI Observations on the Lunar Ephemeris Accuracy. *IAA RAS Transections,40*, 16–21.
6. Folkner, W.M., Williams, J.G., Boggs, D.H., Park, R.S., & Kuchynka, P. (2014). The Planetary and Lunar Ephemerides DE430 and DE431. *IPN Progress Report 42-196*.
7. Marshalov, D.A., Bondarenko, Yu.S., Medvedev, Yu.D., Vavilov, D.E., Zotov, M.B., & Mikhailov, A.G. (2018). A Complex for Carrying Out Radar Observations of Near-Earth Objects. *Instruments and Experimental Techniques, 61* (4) , 577–582.
8. Grenkov, S.A., Nosov, E.V., Fedotov, L.V., & Kol'tsov, N.E. (2010). A Digital Radio Interferometric Data Acquisition System. *Instruments and Experimental Techniques, 53* (5), 675–681.
9. Thomas, J.B. (1989). An Analysis of Digital Phase-Locked Loops. *JPL Publication 89-2*.

10. Vasilyev, M.V., & Yagudina, E.I. (2014). Russian Lunar Ephemeris EPM-ERA 2012. *Solar System Research, 48* (2), 158–165.
11. Krasinsky, G.A., & Vasilyev, M.V. (1997). ERA: Knowledge Base for Ephemeris and Dynamical Astronomy. *IAU Colloquium*, *165*, 239–244.
12. IERS Conventions. (2010). *IERS Technical Note No.36*.
13. Boehm, J., Werl, D., & Schuh, H. (2006). Troposphere Mapping Functions for GPS and Very Long Baseline Interferometry from European Centre for Medium-Range Weather Forecasts Operational Analysis Data. *J. Geophys. Res., 111*, B02406.

TRĪSVIRZIENU MĒNESS RADIO PĀRRAIDES EKSPERIMENTS UZ RT-32 RADIOTELESKOPIEM

D. Maršalovs, Dž. Pings, V. Li, M. Vangs, Dž. Sans,
J. Bondarenko, M. Vasiļjevs, E. Jagudina

K o p s a v i l k u m s

Kopš 2017. gada Krievijas Zinātņu akadēmijas Lietišķās astronomijas institūts sadarbībā ar Ķīnas Zinātņu akadēmijas Nacionālajām astronomiskajām observatorijām veic Chang'E-3 piezemēšanās nesēja viļņa signāla novērojumus. Darbā aprakstītas novērojumu plānošanas iezīmes un datu apstrādes rezultāti. Augstas precizitātes fāzes radara mērījumi tika iegūti ar instrumentālo kļūdu 1–2 mm. Atlikumu novirze modeļa aprēķinos nepārsniedz ± 1 cm. CE-3 piezemēšanās ierīces stāvokļa aprēķini tika iegūti ar precizitāti 0,5‘‘, 7,4 m un 3,2 m attiecīgi celenocentriskā cilindriskā garumā, Px un Py koordinātēs.

Atslēgas vārdi: *Chang'E-3, ciparu fāzes bloķēšanas cilpa, Mēness efemers, Mēness radio diapazons, fāzes mērīšana, radioteleskops*

sciendo

LATVIAN JOURNAL OF PHYSICS
AND TECHNICAL SCIENCES
2020, N 1-2

DOI: 10.2478/lpts-2020-0004

STUDY OF FEED HORN SOLUTIONS FOR IRBENE RT-32 RADIO TELESCOPE

M. Bleiders

Engineering Research Institute
"Ventspils International Radio Astronomy Center",
Ventspils University of Applied Sciences,
101 Inzenieru Str., Ventspils, LV-3601, LATVIA
E-mail: marcis.bleiders@venta.lv

Various feasible solutions of Irbene RT-32 secondary focus feed antennas are designed and compared in the present study. The examined feed antennas include smooth wall and corrugated horns with linear and shaped profiles. Mode matching technique is employed for simulation of scattering parameters and radiation patterns. Genetic algorithm is used for optimisation of horn profile for the best cross-polarization, and aperture efficiency performance. Although the presented horns are valid for any frequency band, different solutions allow choosing the best combination of factors, such as electrical parameters, bandwidth, physical size and complexity of manufacturing.

Keywords: *antenna optimisation, feed horn, Irbene RT-32 radio telescope*

1. INTRODUCTION

Planning has been recently started to expand frequency range of Irbene RT-32 radio telescope by installing new receivers in addition to existing C-X band system. The key component of any reflector antenna receiver system is feed horn, which must be optimised for geometry of specific reflector and it directly affects important performance parameters of the whole radio telescope, such as aperture efficiency, cross-polarization and bandwidth. Although already available C-X band corrugated horn design could be scaled for operation at different frequency bands, in reality it is not always practical. For example, in case of RT-32 geometry, the required feed horn at L and/or S band is physically very large and corrugated design would be expensive and heavy, so smooth wall horn design would be preferred. Even though the existing horn design has almost octave bandwidth with good cross-polarization levels, using careful profile optimisation it is possible to obtain corrugated horn with even better performance, such as the improved aperture efficiency bandwidth. The present paper summarises the initial design of four feasible feed horn options, which include a

smooth wall and corrugated designs with various profile shapes. The whole design process is briefly described, starting from the required performance parameters and ending with discussion about the obtained performance.

2. DESIGN PROCEDURE

Required performance of RT-32 secondary focus feed horn is summarised in Table 1. The main requirement that is set by geometry of RT-32 is a secondary mirror subtended angle and the remaining parameters are either derived from a subtended angle or are rule of thumb values such as amplitude taper at a mirror edge and phase error. The main electrical performance parameters are the maximum cross-polarization level and total illumination efficiency, which must be as good as possible but practically feasible values of better that 20 dB and 60 % respectively are defined.

Table 1

Required Performance of RT-32 Secondary Focus Feed Antenna

Secondary mirror subtended angle	21
Equivalent f/D ratio	2.7
Amplitude edge taper	13 dB
Feed aperture phase error	≈1.3 rad (0.1…0.3)
Main lobe full beam-width	10.6 @ -3 dB, 21 @ -13 dB
Directivity	25 dBi
Maximum cross-polarization level	<-20 dB (>0.99)
Sidelobe level & co-polar beam	<-25 dB, with equal E/H plane patterns
Input return loss	<-25 dB
Illumination efficiency	> 60 %
Fractional bandwidth	> 50 % (octave is 67 %)
Other	Low cost, compact size, small weight

Using the shown requirements of subtended angle, amplitude edge taper and phase error, initial dimensions of conical profile feed horn are estimated using the Gaussian beam technique [1]. The required aperture diameter and slant length to maximise coupling to the fundamental Gaussian beam mode are $a_{app} \approx 3.3\lambda$ and $L \approx 22\lambda$, respectively. Radius of input waveguide a_{in} is set to 0.48λ that is approximately in the middle between TE11 and TM11 mode cut-off wavelengths. The initial profile shape is then parametrized and optimised using a classical genetic algorithm combined with an efficient mode matching technique [2],[3], which was implemented using MATLAB and verified against CST MWO. Overall block diagram of the design algorithm is shown in Fig. 1.

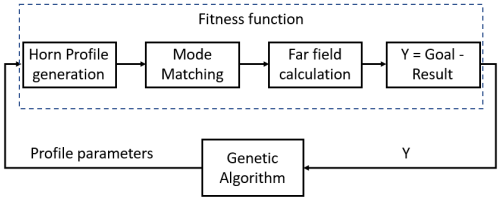

Fig. 1. Block diagram of the employed horn profile optimisation algorithm.

Average of maximum cross-polarization at various frequencies has been used as an optimisation goal in this study, and the goal for the best total illumination efficiency of secondary mirror has been tested with similar results.

3. RESULTS AND DISCUSSION

Resulting profiles of four feasible horns are shown in Fig. 2. Horn #1 is classical Potter dual mode horn with optimised double-step waveguide step structure at input to generate TM11 mode with the correct amount and phase at aperture [4]. Horn #2 is a smooth wall multimode horn with three discrete sections with optimisation carried out on section length and radii of the nodes. Horn #3 is a corrugated horn with a linear conical profile designed according to [5], with additional optimisation carried out on input section, which has gradual change in groove width to improve the bandwidth of return loss [6]. Horn #4 is also a corrugated horn with a similar multiple discrete section profile as #2 but with total length decrease of 30 %. All horns have the same aperture radius of 3.3λ. Typically for genetic algorithm optimisation result to converge, 500–1000 evaluations of fitness function are needed in case of horns #2 and #4, but much less in case of linear profiles #1 and #3.

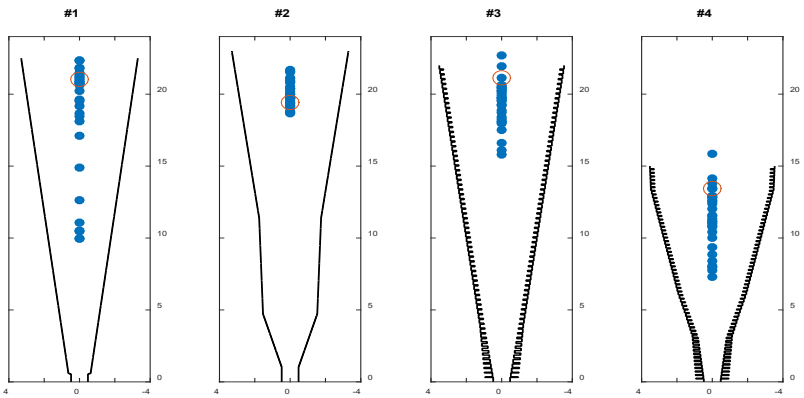

Fig. 2. Optimised profiles of four investigated feed horns. All dimensions are in wavelengths. Dots show phase centre positions at different frequencies (see text).

Normalised frequency dependence of the main performance parameters is shown in Fig. 3. Both corrugated horns have the cross-polarization level better than 20 dB within 67 % (octave) bandwidth reaching levels of 30–50 dB within fractional bandwidth of 47 %. Horn #1 is the narrowest band as expected with cross-polarization reaching 30 dB only at ≈7% wideband around centre frequency. Discrete section smooth wall horn antenna #2 performs similarly to corrugated horns within 14 % of central band with cross-polarization better than 30 dB and better than 20 dB within 50 % bandwidth. All horns have similar 13 dB level beam widths and similar directivities. Input return loss is better than -30 dB above normalised frequency of 0.75 for horns #2 - #4 and better than -20 dB for horn #1. Phase centre positions at multiple frequencies are shown in Fig. 2 with filled dots with highlighted points showing position at central frequency. Surprisingly, horn #2 has the most stable phase centre position.

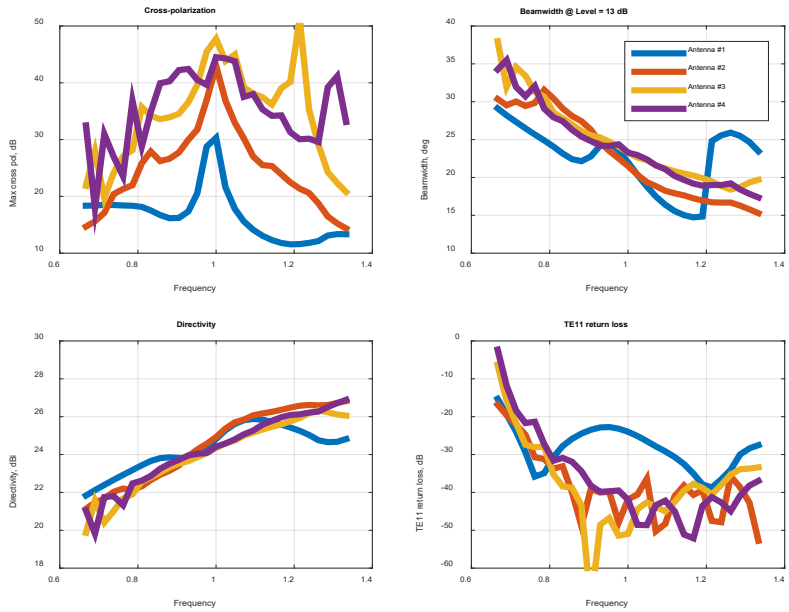

Fig. 3. Maximum cross-polarization level, 13 dB level beam width, directivity and input return loss of the four proposed profiles vs. relative frequency.

Figure 4 shows comparison of total feed efficiency calculated for subtended angle of 21˚, which includes sub-efficiencies of illumination, spill-over, phase, cross-polarization and secondary mirror blockage [7]. Reflector surface and secondary mirror alignment accuracy are not considered in this analysis. All horns reach almost 80 % efficiency near centre frequency with the flattest response in case of corrugated horn #3 and #4. Horn #4 has ≈5 % worse maximum efficiency due to its decreased length and accordingly decreased phase efficiency, which may also cause relatively unstable phase centre position evident in Fig. 2. Corrugated horns #3 and #4 have efficiency better than 60 % and 55 % within octave bandwidth, and smooth profiled horn #2 reaches efficiency better than 60 % within bandwidth of 40 %.

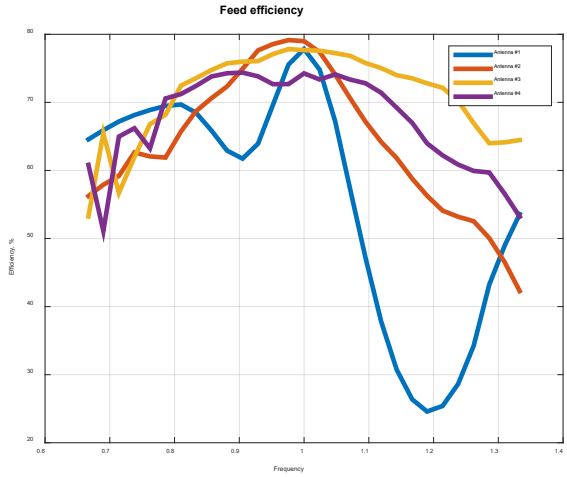

Fig. 4. Total feed efficiency vs. relative frequency in case of RT-32 secondary subtended angle of 21˚.

4. CONCLUSIONS

Four horn profiles have been investigated for possible Irbene RT-32 feed antenna design. Smooth wall Potter profile (antenna #1) is the narrowest band, but at the same time the simplest and most cost-effective option. Good candidate for L/S band feed design is profile #2 due to its relatively low cost and small weight, but efficiency performance is comparable to the corrugated horns. For instance, one could achieve RT-32 feed efficiency better than 50 % with maximum of 79 % within frequencies of 1.2 to 2.32 GHz with a smooth profile horn possibly fabricated from sheet metal with total horn length of 3.67 m and aperture diameter of 1.1 m. For the absolute widest band performance, full length corrugated horn such as #3 is the best option and would be a good solution for RT-32 K band feed design. In this case, efficiency of better than 50 % (neglecting the surface accuracy of RT-32) within 18 to 36 GHz could be achieved, with horn length and aperture diameter of 24 cm and 7.3 cm, respectively. With additional optimisation of horn #3 profile, it may be possible to increase the efficiency at octave band edges even more. Current design of profile #4 has ≈5 % less efficiency in comparison with full length profiles, which in some situations may be outweighed by 30 % smaller physical size.

Further research will be conducted to improve the horn designs and design software. Nevertheless, the current results allow concluding that the currently implemented design techniques are capable for in-house design of high-performance feed horns for Irbene parabolic antennas.

REFERENCES

1. Goldsmith, P. F. (1998). *Quasioptical systems: Gaussian beam quasioptical propagation and applications*. Wiley-IEEE. ISBN: 978-0-7803-3439-7
2. Ruiz-Cruz, J. A., Montejo-Garai, J.R., & Rebollar, J.M. (2010). Computer Aided Design of Waveguide Devices by Mode-Matching Methods. *Passive Microwave Components and Antennas*, 117–140. DOI: 10.5772/9403
3. Polo-Lopez, L., Ruiz-Cruz, J.A., Corcoles, J., & Leal-Sevillano, C.A. (2015). Analysis and Design of Horn Antennas with Arbitrary Profile Using Mode-Matching. In *Congress on Numerical Methods in Engineering, CMN 2015*, 29 June–2 July 2015, Lisbon, Portugal.
4. Potter, P. D. (1963). A New Horn Antenna with Suppressed Sidelobes and Equal Beam Widths. *Microwave J., 6*, 71–78.
5. Clarricoats, P. J. B., & Olver, A. D. (1984). *Corrugated horns for microwave antennas*. The Institution of Engineering and Technology. ISBN: 9780863410031
6. Zhang, X. (1993). Design of Conical Corrugated Feed Horns for Wide-Band High-Frequency Applications. *IEEE Transactions on Microwave Theory and Techniques, 41* (8), 1263–1274. DOI: 10.1109/22.241664
7. Olver, A.D., Clarricoats, P.J., Kishk, A.A., & Shafai, L. (1994). *Microwave horns and feeds*. The Institution of Engineering and Technology. ISBN: 9781849193955

POTENCIĀLU APSTAROTĀJU RISINĀJUMU IZPĒTE PIELIETOJUMAM RT-32 RADIO TELESKOPĀ

M. Bleiders

K o p s a v i l k u m s

Rakstā tiek salīdzināti dažādi sekundārā fokusa apstarotāju antenu risinājumi, kas optimizēti potenciālam pielietojumam Irbenes RT-32 radio teleskopam. Apskatītās antenas ietver ruporantenas ar gludu virsmu, kā arī skalārās ruporantenas ar lineāriem un optimizētas formas profiliem. Ruporantenu izkliedes parametru un izstaroto lauku parametru simulācijām tiek izmantota modālās salāgošanas metode. Ruporantenu profilu optimizācijai tiek izmantots ģenētiskais algoritms, optimizāciju veicot maksimāli augsta ortogonālo polarizāciju atdalījuma līmeņa, stara simetrijas un apertūras efektivitātes iegūšanai. Lai arī apskatītie apstarotāji ir izmantojami jebkuram frekvenču diapazonam, dažādi risinājumi ļauj izvēlēties labāko kompromisu starp elektrisko veiktspēju un mehānisko sarežģītību.

Atslēgas vārdi: *antenu optimizācija, apstarotāja antena, Irbenes RT-32 radio teleskops*

sciendo

LATVIAN JOURNAL OF PHYSICS
AND TECHNICAL SCIENCES
2020, N 1-2

DOI: 10.2478/lpts-2020-0005

THE LOFAR LONG-BASELINE CALIBRATOR SURVEY CLASSIFICATION

A. Nikolajevs, K. Prūsis*

Engineering Research Institute
"Ventspils International Radio Astronomy Center",
Ventspils University of Applied Sciences,
101 Inzenieru Str. 101, Ventspils, LV-3601, LATVIA
*e-mail: kaspars.prusis@venta.lv

Data manipulation of the LOFAR Long-Baseline Calibrator Survey (LBCS) and the Westerbork Northern Sky Survey (WENSS) catalogues are carried out in the present study. The aim of the study is to make calibrator classification statistics plots and estimations for further observations and upcoming stations. First, mean flux densities of LBCS calibrators against declination and observed station baseline length to the tied core station are plotted and the classified sources are marked. Second, we provide the designation – naming it the success rate – for the number of sources with the correlated signal against all the LBCS catalogue sources. Third, there is a trend in mean peak flux densities between stations – longer the baseline, higher mean peak flux density. Finally, estimations for upcoming and recent stations are made and some results are not encouraging.

Keywords: *catalogue manipulation, LBCS classification, LOFAR calibrators, statistical estimation*

1. INTRODUCTION

LOFAR, the LOw-Frequency ARray [1], is a new-generation radio interferometer constructed in the north of the Netherlands and across Europe. LOFAR covers the largely unexplored low-frequency range from 10–240 MHz and provides a number of unique observing capabilities. LOFAR is one of the first radio observatories to feature automated processing pipelines to deliver fully calibrated science products to its user community. New capabilities and techniques of LOFAR make it an important pathfinder for the Square Kilometre Array (SKA) [2].

One of the challenges in the design of the LOFAR radio telescope is calibration of the ionospheric effects as at low frequencies ionosphere is not uniform and can change within minutes [3]. Compensation for phase delays caused by Earth's atmosphere is very important for further radio interferometer data interpretation. To

achieve it, a calibrator source near the target source must be observed. They should be close enough on the sky to be subject to approximately the same propagation effects. To perform calibration, delay and phase solutions are transferred from the calibrator to the target source. The aim of LOFAR LBCS [4] is to identify sources over a large part of the northern sky suitable for calibrating further observations. The survey includes sources with correlated flux densities starting from 50 mJy at frequencies around 110–190 MHz. Suitable sources are described as calibrator density over the sky. For the shortest international baselines, there is around one suitable calibrator source per square degree. For the longest baselines, there are significantly fewer suitable calibrators available. LBCS is an ongoing project and more than 24 000 sources have been observed and processed so far. LBCS database is formed using survey results. For each International LOFAR Telescope (ILT) [5] station, sources are classified into groups that are described if the source can be considered a suitable calibrator (marked as P-class) or there is insufficient correlated flux for calibration (marked as X-class). The LBCS source selection in the region north of 30^{o}N uses three surveys. The first survey is the 74MHz VLSS [6], the second survey is the Multi-frequency Snapshot Sky Survey (MSSS) [7], and the third, the most used one, is the 325 MHz WENSS [8]. The LBCS database does not contain flux densities per beam for each source and the WENSS catalogue can be used to supplement the list. WENSS catalogue [9] sources are observed at frequency different from LBCS but still close enough for further calibrator classification statistics; therefore, estimations can be made.

2. CALIBRATOR CLASSIFICATION ESTIMATION

Automated Python scripts are used to manipulate WENSS and LBCS catalogues. As there are no unified source names in both catalogues, script recognises sources by their coordinates – right ascension and declination. There are 24 893 sources so far in the LBCS and 229 420 sources in the WENSS catalogue. ERI VIRAC high performance computing server cluster is used for execution of the scripts. In total, 18 447 sources overlaid in both catalogues and formed a new list containing LBCS database concatenated with peak flux densities from WENSS catalogue.

This chapter briefly explains catalogue manipulation and statistical methods used to acquire calibrator classification estimation.

Mean flux densities against declination are described in the following section. Peak flux densities are displayed as P-class or X-class source against declination. The script generates plots for every single station. Each source in the plot is displayed as P or X class source (for the specific station). Axes represent peak flux density in mJy/beam and declination in degrees. Range of Y-axis is limited to see only most of the points. Mean values are calculated for short intervals of 10 degrees by calculating all the specific class source peak flux densities in the interval and dividing by the count of sources. Mean values are connected to form a line. We chose to show the most extreme cases – the closest station DE605 (Jülich, 226 km) in Fig. 1 and the furthest station FR606 (Nançay, 700 km) in Fig. 2 to the tied core station at Exloo. Stations of Poland and Ireland were not included due to the lack of observed sources.

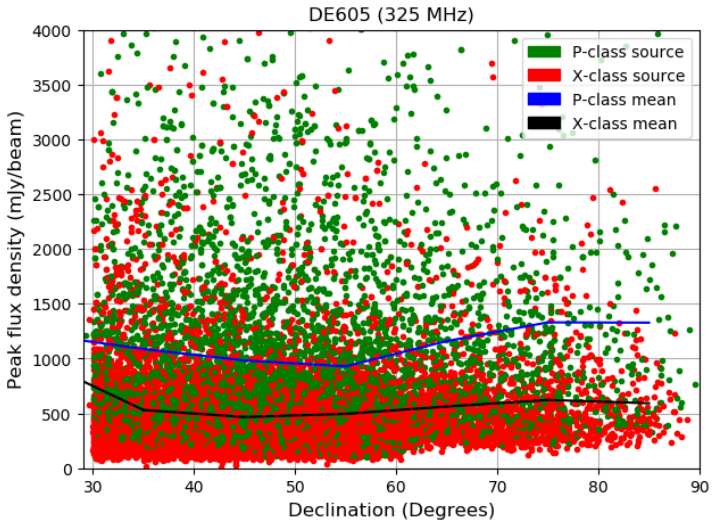

Fig. 1. DE605 peak flux densities and their mean values (classified as LBCS P or X sources) against declination – as the best case.

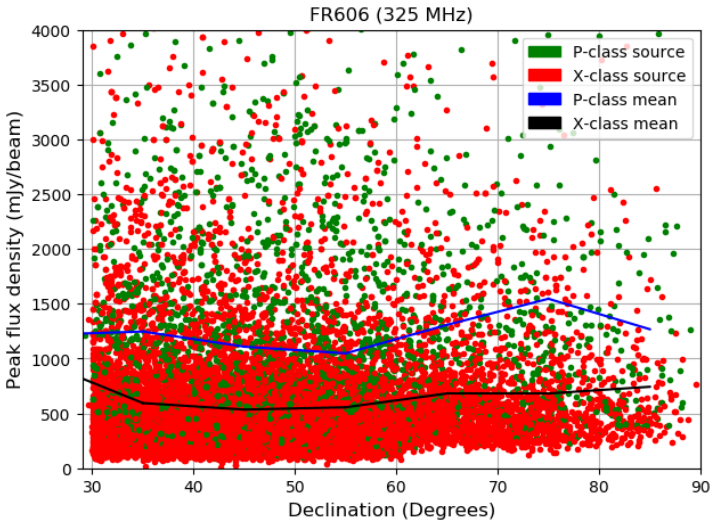

Fig. 2. FR606 peak flux densities and their mean values (classified as LBCS P or X sources) against declination – as the worst case.

Further data acquired on mean flux densities against baselines will be described. The script calculates and generates mean peak flux densities of the P or X class sources for each station. In Fig. 3, axes represent mean peak flux density in mJy/beam and station-to-core baseline length in km. The linear trendline is also marked for the P and X class source data as the points form a significant trend. The linear trendline equation is calculated using *polyfit()* and constructed using *poly1d()* function of *numpy* package.

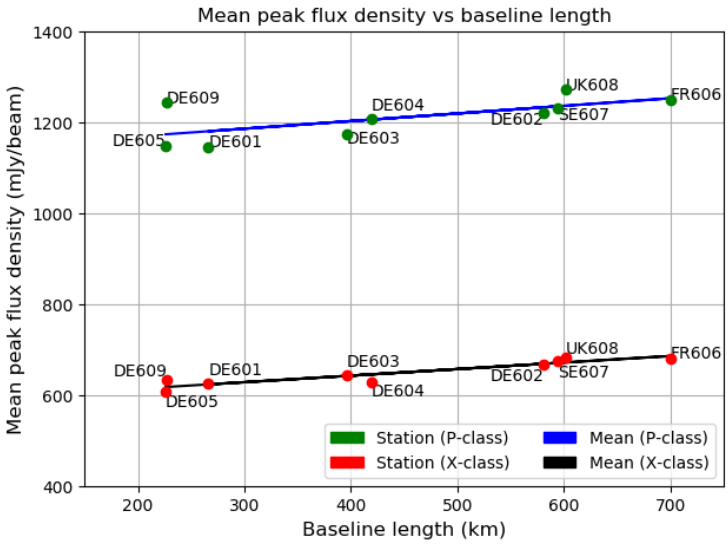

Fig. 3. Mean peak flux densities per station for P and X class sources.

3. RESULTS AND DISCUSSION

Results of mean peak flux densities against declination can be seen in Fig. 1, while Fig. 2 shows the distribution of P (as green dots) and X (as red dots) class sources on the plot. As we can see, there are more red dots at the bottom and occurrence of green dots increases if we move above. If plots were to be compared from different stations, then there would be obviously more red dots than green dots on longer baselines. The mean line on the plot shows mean peak flux density on a specific declination interval. Peak flux density decreases as we move further in declination till 60 degrees. Above 60 degrees there is a gap of sources at a lower limit of the plot. It results in an increase in mean values at the declination range. For all the stations used in the LBCS observations, the mean peak flux density trend is very similar. For longer baselines mean lines move up slightly.

In Fig. 3, we can see a significant trend for both P and X class source data. Mean values are about 1150 mJy/beam for the shortest baseline stations (DE605, DE601) of P-class source data. The last station in the plot (FR606) has the mean peak flux density around 1250 mJy/beam. A similar trend can also be observed for X-class source data – just above 600 mJy/beam and 700 mJy/beam, respectively. Resulting P-class source (1) and X-class source trendline equations (2) are as follows:

$$MPFD = 0.1672 \cdot BL + 1135.33 \quad (1)$$

$$MPFD = 0.1439 \cdot BL + 584.86 \quad (2)$$

where $MPFD$ – mean peak flux density, mJy/beam;

BL – baseline length to the tied core station, km.

We can statistically estimate from trendlines what mean peak flux density is more likely to be from P or X class source for a certain baseline length. There are more recent international stations that are not included in Table 1. Knowing their baseline length to the tied core station, we can calculate what mean peak flux density sources are more likely to be suitable as calibrators. There are five international stations – PL610 (693 km), PL611 (999 km), PL612 (915 km), IE613 (989 km) –, and an upcoming station in Latvia LV614 (1079 km).

Table 1

Mean Peak Flux Density Estimation for Recent Stations

International station	Baseline length to the tied core station (km)[1]	Estimated mean P class source peak flux density (mJy/beam)	Estimated mean X class source peak flux density (mJy/beam)
PL610	693	1251	685
PL611	999	1302	729
PL612	915	1288	717
IE613	989	1301	727
LV614	1079	1316	740

4. CONCLUSIONS

Statistically, the mean peak flux density is lower for the sources on higher declination. It might be affected by the ionosphere because the layer of the ionosphere is thicker on lower elevation (and also declination). Another reason might be a man-made interference because observing at a lower declination station will detect manmade radio signals from the ground. Longer baselines statistically should have higher flux density to classify the source as P class.

In Fig. 3, there is just a small difference between the shortest and the longest baseline mean peak flux densities, but it is worth mentioning. Even the estimated data for the furthest station LV614 do not differ significantly. However, the change between baseline lengths may hold useful information about P and X class estimation.

The estimation of good calibrator sources (success rate) for baselines has also been performed. It has demonstrated that there is a huge contrast between stations when we compare the success rate. The designation reflects the number of LBCS calibrators that can be used to calibrate a baseline with a certain length. Unfortunately, the result is not encouraging for some recent or upcoming stations. The shortest baseline station (DE605) success is rated as high as 70 % but at the moment the longest baseline station (PL611) has only 3 %. It seems that there may not be any LBCS calibrator for upcoming station LV614. Therefore, we need solutions, such as another calibrator survey with more compact sources.

ACKNOWLEDGEMENTS

We would like to thank Dr Neal Jackson from Jodrell Bank Centre for Astrophysics (JBCA), Manchester, the United Kingdom, for his great help in providing theoretical basis in radio interferometry and providing assistance in LOFAR data processing. Our recent study in this area has been supported by project No. 692257 – BALTICS (Building on Advanced LOFAR Technology for Innovation, Collaboration, and Sustainability).

REFERENCES

1. van Haarlem, M.Á., Wise, M.W., Gunst, A.W., Heald, G., McKean, J.P., Hessels, J.W.T., ... & Brentjens, M. (2013). LOFAR: The Low-Frequency Array. *Astronomy & Astrophysics*, *556*, A2. DOI: 10.1051/0004-6361/201220873
2. Dewdney, P., Hall, P., Schillizzi, R., & Lazio, J. (2009). The Square Kilometre Array. *Proceedings of the Institute of Electrical and Electronics Engineers IEEE*, *97* (8), 1482–1496. DOI: 10.1017/pasa.2012.007
3. van der Tol, S., & van der Veen, A. J. (2007, July). Ionospheric Calibration for the LOFAR Radio Telescope. In *2007 International Symposium on Signals, Circuits and Systems* (vol. 2, pp. 1–4). IEEE. DOI: 10.1109/ISSCS.2007.4292761
4. Jackson, N., Tagore, A., Deller, A., Moldón, J., Varenius, E., Morabito, L., ... & Kapinska, A. (2016). LBCS: The LOFAR Long-Baseline Calibrator Survey. *Astronomy & Astrophysics*, *595*, A86. DOI: 10.1051/0004-6361/201629016
5. Vermeulen, R. C., & Van Haarlem, M. (2011, August). The International LOFAR Telescope (ILT). In *2011 XXXth URSI General Assembly and Scientific Symposium* (pp. 1–1). IEEE. DOI: 10.1109/URSIGASS.2011.6051244
6. Lane, W. M., Cotton, W. D., van Velzen, S., Clarke, T. E., Kassim, N. E., Helmboldt, J. F., ... & Cohen, A. S. (2014). The Very Large Array Low-Frequency Sky Survey Redux (VLSSr). *Monthly Notices of the Royal Astronomical Society*, *440*(1), 327–338. DOI: 10.1093/mnras/stu256
7. Heald, G. H., Pizzo, R. F., Orrú, E., Breton, R. P., Carbone, D., Ferrari, C., ... & Rafferty, D. (2015). The LOFAR Multifrequency Snapshot Sky Survey (MSSS)-I. Survey Description and First Results. *Astronomy & Astrophysics, 582*, A123. DOI: 10.1051/0004-6361/201425210
8. Rengelink, R. B., Tang, Y., De Bruyn, A. G., Miley, G. K., Bremer, M. N., Roettgering, H. J. A., & Bremer, M. A. R. (1997). The Westerbork Northern Sky Survey (WENSS)-I. A 570 square degree Mini-Survey around the North Ecliptic Pole. *Astronomy and Astrophysics Supplement Series, 124* (2), 259–280. DOI: 10.1051/aas:1997358
9. Browse Software Development Team. (2006). *WENSS (Westerbork Northern Sky Survey) Radio Catalogue*. Available at https://heasarc.gsfc.nasa.gov/W3Browse/radio-catalog/wenss.html

LOFAR GARO BĀZES LĪNIJU KALIBRATORU SESIJAS KLASIFIKĀCIJA

A. Nikolajevs, K. Prūsis

K o p s a v i l k u m s

Šajā dokumentā ir aprakstīta LOFAR garo bāzes līniju kalibratoru sesijas (LBCS) un Vesterborkas ziemeļu debess novērojumu (WENSS) sesiju datu apstrāde. Darba mērķis ir izveidot kalibratoru klasifikācijas grafikus un novērtējumus turpmākajiem novērojumiem un gaidāmajām stacijām. Pirmkārt, vidējie LBCS kalibratoru plūsmas blīvumi pret deklināciju un stacijas bāzeslīnijas garumu līdz tīkla centra stacijai ir attēloti un klasificētie avoti ir iezīmēti. Otrkārt, mēs piedāvājam apzīmējumu – pozitīvo rezultātu daudzums – kas ir novēroto avotu skaits, kuriem veidojas korelētais signāls attiecībā pret visiem LBCS kataloga avotiem. Treškārt, pastāv tendence vidējo pīķa plūsmas blīvumos starp stacijām - jo garāka bāzes līnija, jo augstāks vidējais pīķa plūsmas blīvums. Visbeidzot, tiek veikts gaidāmo un neseno staciju novērtējums, un daži rezultāti nav iepriecinoši.

Atslēgas vārdi: *LOFAR kalibratori, LBCS klasifikācija, statistiskie novērtējumi, katalogu manipulācija*

sciendo

LATVIAN JOURNAL OF PHYSICS
AND TECHNICAL SCIENCES
2020, N 1-2

DOI: 10.2478/lpts-2020-0006

DATA REDUCTION AND IMAGING OF GRAVITATIONAL LENS SYSTEM CLASS B0631+519

K. Prūsis*, A. Nikolajevs

Engineering Research Institute
"Ventspils International Radio Astronomy Center",
Ventspils University of Applied Sciences,
101 Inzenieru Str., Ventspils, LV-3601, LATVIA
*e-mail: kaspars.prusis@venta.lv

The present paper describes reduction procedures and imaging of radio astronomical data from the gravitational lens system CLASS B0631+519 acquired by e-MERLIN interferometer. The source has been previously imaged with VLA, MERLIN and the VLBA interferometers. Data reduction and polarisation calibration procedures will provide data on Faraday effects such as Faraday rotation and depolarization between lensed images that in turn carry information on large and small-scale magnetic fields in the lensing galaxy.

Reduction of data and imaging of the radio astronomical source have been achieved using Astronomical Image Processing System (AIPS) in conjunction with automatic data reduction pipelines that performed specific data processing steps. As a result, the sky map for the gravitational lens system has been successfully acquired and accuracy comparing the generated map to sky maps of the source produced by different authors has been confirmed.

Keywords: *AIPS, gravitational lensing, Parseltongue, SERPent*

1. INTRODUCTION

Strong gravitational lensing is a phenomenon when a background source obscured by a massive galaxy or a cluster of galaxies is multiply imaged and visible in the field of site besides the intervening or lensing galaxy. It is caused by the gravitational field of the intervening galaxy that effectively bends the ray-path emitted by background source [1]. A visual representation of basic gravitational lensing is shown in Fig. 1.

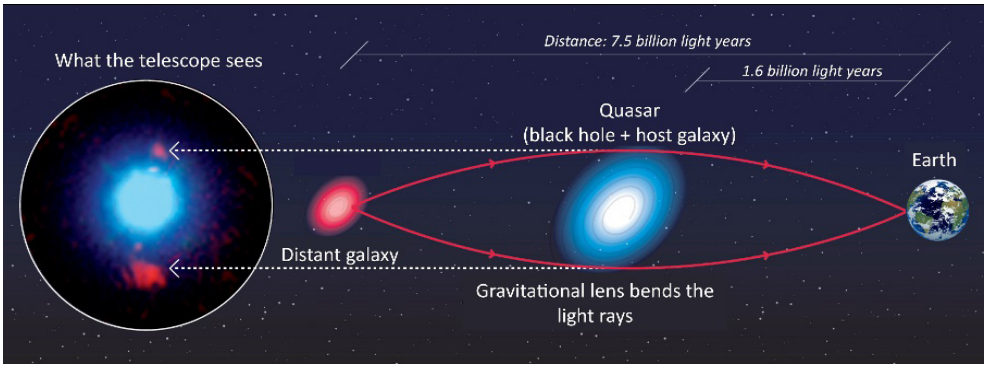

Fig. 1. Image describing principles of gravitational lensing. The image itself is of the quasar SDSS J0013+1523 (blue), bracketed by the lensed images of the background galaxy (red), obtained with the W. M. Keck Observatory's 10 m telescope and Adaptive Optics. From "Caltech / EPFL / WMKO" by F. Courbin, S. G. Djorgovski, G. Meylan, et al., 2010, http://www.astro.caltech.edu/~george/qsolens/lensillustration.jpg.

CLASS B0631+519 (Fig. 2) has one of the richest lensed image structures known and is thus an ideal system to probe mass properties of the lensing galaxy, including Faraday rotation and depolarization between lensed images to determine large and small-scale magnetic fields in the lensing galaxy. Unlike the standard Faraday rotation measure grid technique, the lensing approach can deliver Faraday rotation and Faraday dispersion produced by a distant intervening galaxy free of contamination from the background source and the Milky Way. [2]

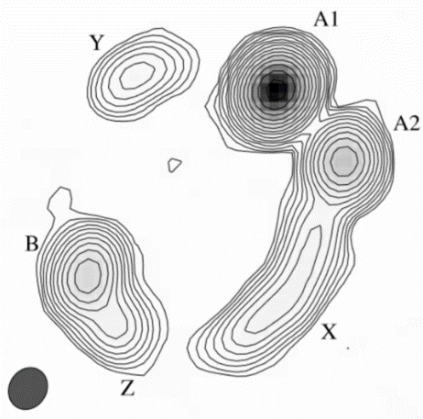

Fig. 2. Radio map of the 1.7 GHz MERLIN observations taken on 1 March 2003. The data were naturally weighted. The synthesized beam is sized 186×161 mas at P.A. −31.7◦. Contours are plotted at factors of (-3, 3, 4.5, 6.75, 10.1, 15.2, 22.8, 34.2, 51.3, 76.9, 115, 173, 259, 389, 584, 876) times the RMS noise [1].

In order to obtain information on Faraday effects, extensive processing of raw correlated data must be performed to acquire the image of the galaxy and perform polarization calibration (see Fig. 3) [3]–[5].

A full process starting from signal detection and ending with the generation of an image of a radio astronomical source is shown in Fig. 3. The data processing steps covered in green have been performed by the authors and are described in the paper.

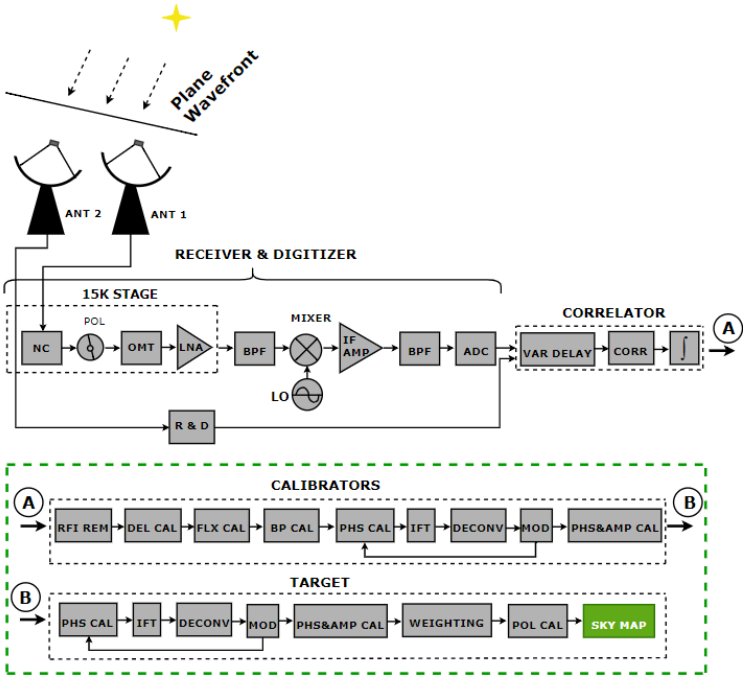

Fig. 3. Diagram of the approximate hardware and software needed to obtain an image of an astronomical source from signals detected by radio telescopes.

The following parts of the paper provide a deeper explanation of specific procedures and tools needed to obtain sky maps of astronomical objects. The results of data processing for CLASS B063+519 data are also given.

2. E-MERLIN DATA FORMAT

CLASS B0631+519 was observed and correlated using e-MERLIN radio interferometer, consisting of 7 telescopes (21 baseline in total) [6] and operating in standard continuum mode:

- Data were split into 8 sub-bands (called IFs);
- Each sub-band was 64 MHz wide (8 by 64 MHz = 512 MHz/BW), divided into 512 spectral channels;
- Observed bandwidth was 1250–1750 MHz;
- Expected RMS noise for a 12 hr on-source observation run: 6 μJy/beam, twice this value if Lovell telescope was not included [7].

After observation, the correlated data were exported to a FITS-IDI standard file format. For a given observing run, each FITS file contained a single source, with multiple sub-bands per FITS file if these sub-bands were spectrally identical. The FITS-IDI data were hosted at Jodrell Bank Observatory (JBO) close to the correlator on archive disks [7].

Usually, a number of sources including the target are observed as part of the run because multiple sources need to be observed to perform calibration procedures for radio telescopes. The observation consists of scans from:

1. The target source (in particular case B0631+519);
2. The phase calibrator (PH-Cal) – 0631+531;
3. An absolute flux calibrator (FX-Cal) – 3C286 (1331+305);
4. A bright point-source calibrator (PT-Cal) – OQ208 (1407+286);
5. A zero-polarization calibrator (ZEROPOL-Cal) – 3C84 (0319+415);
6. An absolute position angle calibrator (ANGPOL-Cal) – 3C286 (1331+305).

The 25-hour observation is mainly structured in ~10 minute cycles, where approximately 3 minute PH-Cal scans are followed by ~7 minute scans on the target supplemented with an hour or 2 hour long observations for other calibrators.

3. DATA PROCESSING

Data processing was carried out according to the guidelines provided in *e-MERLIN COOKBOOK* [7]. To perform data processing, a partly automated software *eMERLIN pipeline.py* [8] was used. Scripted E-merlin RFI-mitigation Pipeline for interferometry (SERPent) [9] was also utilised. The aim of these pipelines is to reduce the data processing burden for scientists and to reduce time required for data processing. It is very useful because some data processing steps can take up to several weeks when done manually. The pipelines were run using Parseltongue – a Python scripting interface for AIPS [10].

In order to make sure that any data processing steps had been successful, data had to be manually viewed for each baseline (21), both circular polarisations (RR and LL) and for each source. It means that after each data processing step at least 108 manual data viewing procedures had to be performed meaning that even with partial automation provided, still a large amount of time had to be spent to assure data quality.

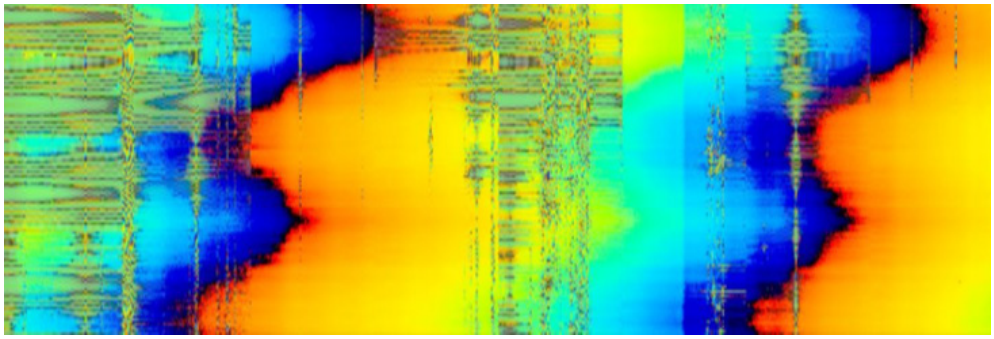

Fig. 4. An image acquired by AIPS task SPFLG for baseline Kn – Da showing data for PT-Cal. All 8 IFs are plotted. X-axis represents frequency, Y-axis represents signal frequency and colour represents the phase of the correlated signal.

In Fig. 4, clear signs of high amplitude RFI can be seen as random phases at particular frequency channels. The amplitudes of uncalibrated data vary between a few 100 μJy to about 1 milliJy [7] but the amplitudes of RFI can reach up to hundreds of Jy.

This RFI is created mainly by transmitters used in communication systems and dominates over the true source signal and after averaging the data can ultimately destroy the coherency of data meaning that reconstruction of the source image is no longer possible. For this reason, to remove RFI, SERPent pipeline together with manual flagging was applied to all the sources, baselines, IFs and time ranges.

In Fig. 4, one can also see a gradual change in phase both in frequency and time. These are called delays or delay offsets. The phase of the interferometer is a function of the frequency multiplied by the delay, meaning delay offsets will show up as a phase slope across the frequency band. Furthermore, if the delay offset changes with time, so will the phase slope, resulting in an additional change in phase as a function of time known as the fringe rate [11], [12].

As stated in [11], there is a large number of ways in which the model used by the correlator can have errors, including errors in the source or antenna positions used, errors in the Earth model, errors in the clock epoch and rate at each antenna and errors in the atmospheric model. Correction of correlator model errors allows the data to be averaged in time and frequency, greatly reducing their volume.

Delay offsets for e-MERLIN data vary from couple up to few hundred nanoseconds and are generally larger on longer baselines. These delays can vary in time, either as gradual drifts, as fibres change temperature and length (note: 1 foot of length change corresponds to 1 nanosecond delay), or occasionally as sharp changes originating in the correlator [6]. If the delays and rates are very rapid after averaging, the coherency of the data may be destroyed. That is why delays have to be corrected as a function of time, which is performed by AIPS task FRING [7].

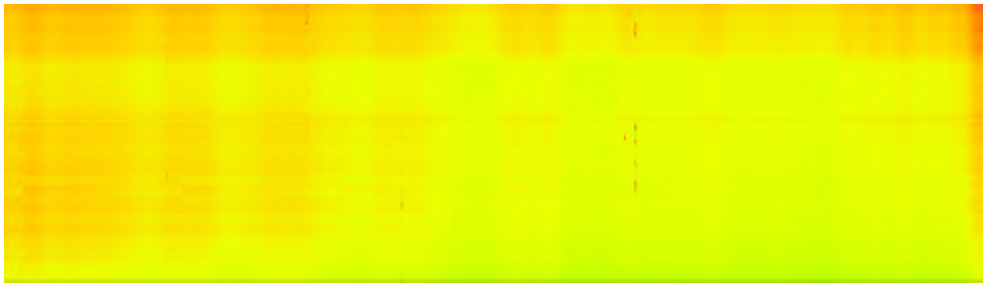

Fig. 5. Phase plot of correlated data for MK2-CM baseline after fringe fitting.

As can be seen in Fig. 5, delays and rates were successfully removed by AIPS task FRING (in contrast to Fig. 4 no phase slope in frequency and time is present). The delay correction must be performed on all calibrators and might need to be run multiple times to correct smaller delays for shorter baselines and larger delays that might be incurred on the longest baselines.

Finally, after carrying out calibration procedures for all calibrators the image generation procedures for the target source are presented.

In order to perform imaging procedures, numerous sets of parameters must be set within AIPS. One of these is the *cell size* parameter that corresponds and should be set to the maximum resolution of an interferometer.

In general, the resolution or synthesized beam width of an interferometer is calculated as $\Omega = \lambda/D$ where D is the maximum separation between two antennas and λ is the wavelength. Maximum distance expressed in wavelengths D_λ can be easily found using AIPS task UVPLT and in this case $D_\lambda \approx 1.3 \cdot 10^6$. Knowing this parameter, a resolution of an interferometer can be expressed as $\Omega \approx 1/D_\lambda$ and the resolution was calculated to be Ω = 158.67 milliarcseconds (mas).

Then 2D Inverse Fourier Transform (IFT) procedure was performed to transform data from Fourier domain to real plane. The first image that is acquired after 2D IFT procedure is called the "dirty image" because in this image the true source brightness is convolved with the PSF of the interferometer [13], [14]. The dirty image of the target source acquired after 2D IFT is shown in Fig. 6.

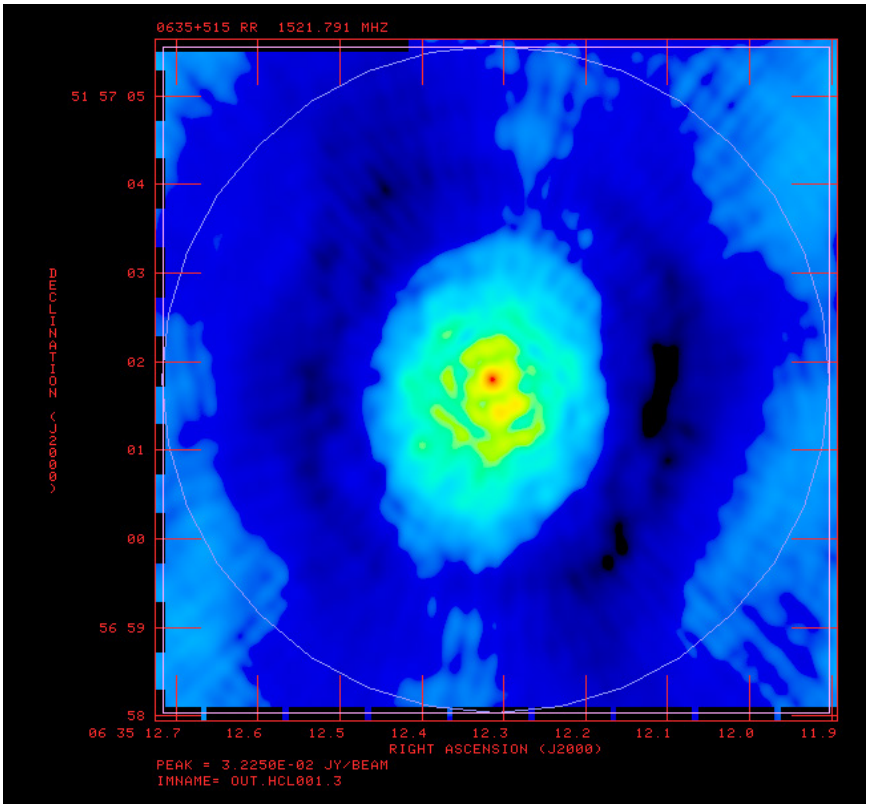

Fig. 6. The "dirty" image of the target source B0635+519 after the first 2D IFT cycle.

Looking at Fig. 6 only a partial source structure is visible compared to Fig. 2, which clearly indicates that true source brightness is convolved by the PSF of an interferometer.

In order to remove the effects of interferometer PSF, a deconvolution algorithm CLEAN implemented in AIPS was used [14].

During the execution of CLEAN algorithm, the coordinates of the maximum amplitude signal were searched in the sky map. When this position was found, a "component" (a spike at this position) was generated of some fraction (called the "gain") of the maximum in the image. This component was then convolved with the PSF of an interferometer and subtracted from the image. The subtracted components are also called "clean" components. This process was done for all the parts of the image and was iteratively repeated until the signal level of the map reached the minimum signal value set. After the process finished, an empty map was generated and collection of clean components was added to this map. They were convolved not with an instrumental PSF but with a more appropriate function, such as a Gaussian [13].

The sky map generated after the first CLEAN cycle is shown in Fig. 7.

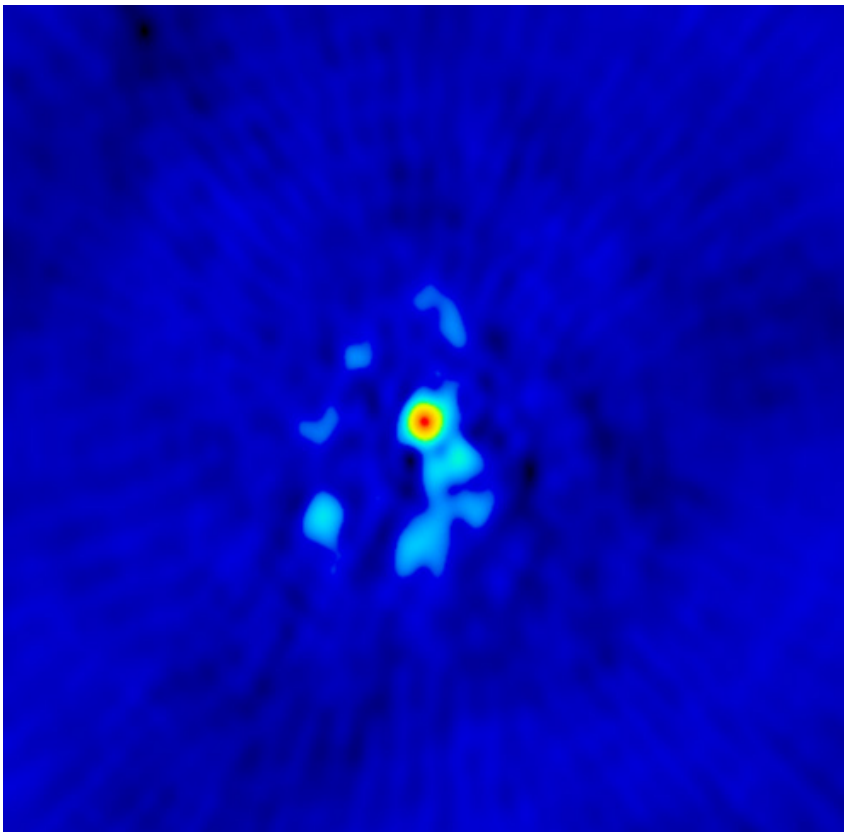

Fig. 7. The image of the target source B0635+519 after the first CLEAN deconvolution cycle.

In the sky map obtained for the target in Fig. 7, a clearer source structure was starting to emerge that better resembled the source structure in Fig. 2. However, further data processing cycles were needed to improve the image quality.

In order to acquire a precise sky map of the target, a self-calibration procedure was performed.

Self-calibration is a process that calculates telescope gains by comparing the observed data with a model of the sky. These gains are used to provide a corrected

dataset, and hence a corrected image, and using this image the process can be repeated iteratively until convergence. The model is provided by the image produced from the data itself, hence, the "self" calibration – and in particular by the clean components (CC) table attached to the image. The procedure is carried out until data convergence is found [7], [15].

The target image obtained in Fig. 7 was used as a model for self-calibration cycles and this procedure was performed until data convergence and minimal noise level in the image were achieved. The final sky map of the target source after multiple phase and amplitude self-calibration cycles is shown in Fig. 8.

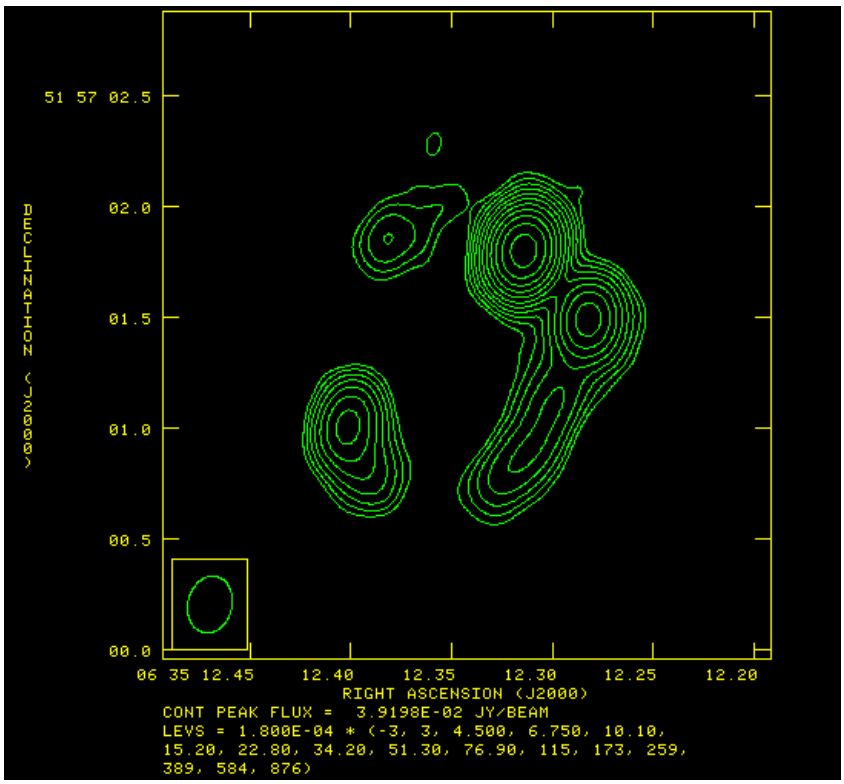

Fig. 8. A sky map of the target source B0635+519 after the 4th self-calibration cycle. The image is contour plotted using AIPS task KNTR. Contours are plotted at factors of (-3, 3, 4.5, 6.75, 10.1, 15.2, 22.8, 34.2, 51.3, 76.9, 115, 173, 259, 389) times the RMS noise ($-1.8e^{-04}$ Jy).

4. CONCLUSIONS

Radio astronomical data reduction is an extensive, time-consuming and complex multi-step process involving various data processing tools and software. For example, when doing reduction for data acquired by e-MERLIN radio interferometer and performing diagnostic tests, information needs to be inspected for 21 baselines, where data are split into 2 circular polarisations, 8 sub-bands and multiple time periods, which resulted in the processing of more than 300 data chunks in one data reduction step.

Nevertheless, numerous automated data processing pipelines and scripting interfaces, including e-MERLIN pipeline, SERPent and Parseltongue etc., have been introduced to remove data processing burden from scientists and to increase the speed of data reduction. While it greatly aids data reduction extensive manual processing, inspection still must be carried out leaving space for future improvements in data reduction automation.

Data reduction and calibration of e-MERLIN data for gravitational lens system CLASS B0631+519 performed by the authors have successfully been executed and the sky map of the object obtained. The RMS noise achieved in the image has been 180 μJy/beam and the total cleaned flux density has resulted in 66.8 mJy which coincides with information available in NASA/IPAC Extragalactic Database (NED) [16] and results provided in [1].

As a whole, acquired knowledge in radio astronomical data processing and various data processing tools will allow VIRAC to participate in future collaborative scientific research concerning corresponding fields of science as well as to perform reduction of data acquired by VIRAC radio telescopes RT-32 and RT-16 not only in single station mode but also when interferometer network is formed, thus expanding VIRAC technological and scientific potential.

Further research must be conducted to perform polarization calibration in order to acquire information about Faraday rotation and depolarization between lensed images that in turn carry information on large and small-scale magnetic fields in the lensing galaxy.

ACKNOWLEDGEMENTS

The authors would like to thank Neal Jackson from Jodrell Bank Centre for Astrophysics (JBCA), Manchester, the UK, for his great help in providing theoretical basis in radio interferometry and giving assistance in data reduction process. The research has used data from the observations with the e-MERLIN that is a UK National Facility operated by the University of Manchester on behalf of Science and Technology Facilities Council (STFC).

Our recent work in this area has been supported by project No. 692257 – BALTICS (Building on Advanced LOFAR Technology for Innovation, Collaboration, and Sustainability).

REFERENCES

1. York, T., Jackson, N., Browne, I.W.A., Koopmans, L.V.E., McKean, J.P., Norbury, M.A., … & Wilkinson, P.N. (2005). CLASS B0631 + 519 : Last of the Cosmic Lens All-Sky Survey Lenses. *Monthly Notices of the Royal Astronomical Society*, *361* (1), 259–271.
2. Mao, S.A., Carilli, C., Gaensler, B.M., Wucknitz, O., Keeton, C., Basu, A., … & Zweibel, E. (2017). Detection of Microgauss Coherent Magnetic Fields in a Galaxy Five Billion Years Ago. *Nature Astronomy*, *1* (9), 621–626.
3. Schwab, F.R., & Cotton, W.D. (1983). Global Fringe Search Techniques for VLBI. *The Astronomical Journal*, *88*, 688.

4. Wrobel, J.M., & Ulvestad, J.S. (1999). Very Long Baseline Array Observational Status Summary. *NRAO*.
5. Hogbom, W.N., Brouw, J.A. (1974). The Synthesis Radio Telescope at Westerbork. Principles of Operation, Performance and Data Reduction. *Astron. Astrophys.*, *33*, 289–301.
6. Garrington, S.T., Anderson, B., Baines, C., Battilana, J.A., Bentley, M.N., Brown D., … & Thomasson, P. (2004). e-MERLIN. *Ground-based Telescopes*, *5489*, 332–344. Belles, P.E., Beswick, R., Argo, M., Jackson, N., Muxlow, T., & Richards, A. (2015). e-MERLIN CookBook. *JBCO*.
7. Argo, M.K. (2015). The e-MERLIN Data Reduction Pipeline. *J. Open Res. Softw.*, *3*, 692257.
8. Peck, L.W., & Fenech, D.M. (2013). SERPent: Automated Reduction and RFI-Mitigation Software for e-MERLIN. *Astron. Comput.*, *2*, 54–66.
9. Kettenis, M., van Langevelde, H. J., Reynolds, C., & Cotton, B. (2006). ParselTongue: AIPS Talking Python. *Astron. Data Anal. Softw. Syst. XV ASP Conf. Ser.*, *351*, 497–500.
10. Cotton, W.D. (1995). Fringe-Fitting. *Very Long Baseline Interferometry and the VLBA*, *82*, 189–208.
11. Morford, J.C. (2017). *The e-MERLIN L-band Legacy Survey of Cygnus OB2*. University College London.
12. Clark, B.G. (1980). An Efficient Implementation of the Algorithm 'CLEAN'. *Astron. Astrophys.*, *89* (3), 377–378.
13. Cornwell, T.J. (2008). Multiscale CLEAN Deconvolution of Radio Synthesis Images. *IEEE J. Sel. Top. Signal Process*, *2*, (5), 793–801.
14. Pearson, T.J., & Readhead, A.C.S. (1984). Image Formation by Self-Calibration in Radio Astronomy. *Annu. Rev. Astron. Astrophys.*, *22*, 97–130.
15. NASA/IPAC Extragalactic Database. (2019). Available at https://ned.ipac.caltech.edu/cgi-bin/datasearch?search_type=Photo_id&objid=8783263&objname=CLASS B0631%2B519%3A%5BYJB2005%5D A1&img_stamp=YES&hconst=73.0&omegam =0.27&omegav=0.73&corr_z=1&of=table#No4

GRAVITĀCIJAS LĒCU SISTĒMAS CLASS B0631+519 DATU APSTRĀDE UN ATTĒLVEIDE

K. Prūsis, A. Nikolajevs

K o p s a v i l k u m s

Rakstā tiek aprakstīts ar e-MERLIN interferometru iegūto gravitācijas lēcu sistēmas CLASS B0631+519 datu apstrādes un attēlveides process.

Iepriekšējie gravitācijas lēcu sistēmas novērojumi ir veikti, izmantojot VLA, MERLIN un VLBI interferometrus.

Datu apstrādes un polarizācijas kalibrācijas procedūras sniegs datus par Faradeja efektiem, piemēram, Faradeja rotāciju un depolarizāciju starp lēcu attēliem, kas savukārt satur informāciju par maza un liela mēroga magnētiskajiem laukiem lēcu galaktikā.

Datu apstrāde un debess ķermeņa attēlveide tika veikta, izmantojot astronomisko datu apstrādes sistēmu AIPS apvienojumā ar dažādām automātiskajām datu apstrādes programmām, kuras veica konkrētus datu apstrādes soļus.

Rezultātā veiksmīgi tika iegūta gravitācijas lēcu sistēmas debess karte, un iegūtās kartes patiesums tika apstiprināts, salīdzinot to ar citu autoru iegūtajām gravitācijas lēcu sistēmas debess kartēm.

Iegūtās zināšanas radioastronomisko datu apstrādē un pieredze darbā ar dažādām astronomisko datu apstrādes programmām ļaus VSRC nākotnē piedalīties kopīgos zinātniskajos pētījumos, kā arī ļaus veikt ar VSRC rīcībā esošo RT-32 un RT-16 radioteleskopu iegūto datu apstrādi ne tikai vienas antenas režīmā, bet arī interferometrijas režīmā, tādējādi paplašinot VSRC tehnoloģisko un zinātnisko potenciālu.

Atslēgas vārdi: *AIPS, gravitācijas lēcas, Parseltongue, SERPent*

sciendo

LATVIAN JOURNAL OF PHYSICS
AND TECHNICAL SCIENCES
2020, N 1-2

DOI: 10.2478/lpts-2020-0007

INFORMATION SYSTEM CYBER THREATS AND TELECOMMUNICATIONS ENGINEERING COURSES

M. Sneps-Sneppe[1]*, D. Namiot[2]**, R. Pauliks[1]***

[1] Ventspils International Radio Astronomy Centre,
Ventspils University of Applied Sciences,
101 Inzenieru Str., Ventspils, LV-3601, LATVIA
*e-mail: manfredss@venta.lv
***e-mail: romass@venta.lv

[2] Faculty of Computational Mathematics and Cybernetics,
Lomonosov Moscow State University,
1 Leninskiye Gory, Moscow, 119991 RUSSIA
**e-mail: dnamiot@gmail.com

The article discusses the issue of training of telecommunications engineers. The architecture of telecommunications solutions is changing very quickly. Obviously, training programmes must also change. Cybersecurity issues are one of the main drivers of change in telecommunications solutions and, therefore, training programmes. They have become the main issues in all processes related to digital transformation. At the same time, it is clear that the development of education in telecommunications clearly lags behind modern requirements. Such issues come to the fore in relation to the development of digital economy programmes. Cyber security issues for military telecommunications solutions are discussed separately.

Keywords: cybersecurity, education, telecom

1. INTRODUCTION

Several trends have shaped the telecommunications industry over the past few years. Most prominent examples, such as Software Defined Networks (SDN), Network Function Virtualization (NFV), Artificial Intelligence (AI), Internet of Things (IoT), and mobile technology 5G, show a growing number of connected devices and the increasing importance of the software. The knowledge of these trends is expected from graduates of telecommunications study programmes.

The paper is initiated by the approach to telecommunications engineer education developed at the University of Applied Sciences, FH Campus Wien [1]. In [1], the new study degree programme “Computer Science and Digital Communications”

(hereinafter Vienna Programme) is offered. During the first three semesters, students obtain a solid basis in mathematics, programming and communication networks as well as fundamentals in telecommunications, security and software engineering. Four free elective modules in 4th and 5th semesters are introduced, namely:

- Micro-Controller for low-level programming skills;
- Software Systems for high-level programming and AI skills;
- Modern Networks for telecommunications and IoT skills;
- IT-Security for cryptography and cybersecurity skills.

The aim of the present study is to evaluate whether education changes proposed by the Vienna Programme are reasonable and justified. In the study, we focus on Information System issues. The rest of the paper is organised as follows. In Section 2, we discuss telecom fraud and telecom architectures. In Section 3, we target military communications. Section 4 is devoted to conclusions.

2. EVOLUTION OF TELECOM FRAUD

Cybersecurity and Telecommunications generally go hand in hand. Many of the targets of cybercrime are focused around the telecoms industry. As advanced technology changes the way telecoms companies run business, cybersecurity also needs to increase [2].

Understanding of the current threat landscape in the field of telecommunications can help reduce the impact of crime like telecom fraud and prepare us for future threats in the age of the IoT. The annual cost of telecommunications subscription fraud is estimated up to more than US$12 billion, while others foresee the actual losses to be far greater, between 3 percent and 10 percent of the operators' gross revenues [3].

Circuit Switching. The older type of telecom network design is circuit-switched technology, which is similar to the one that was once used by human switchboard operators. These switchboard operators would verbally ask who the call was for and manually plug cables into a switchboard to establish the connection (the circuit). Eventually, the human switchboard operators were replaced by automated machines, but the technology design was effectively unchanged for a hundred years (Fig. 1). A very common vulnerability in these networks was that the switchboard operators would listen to the conversations of all the most interesting people in the city [4].

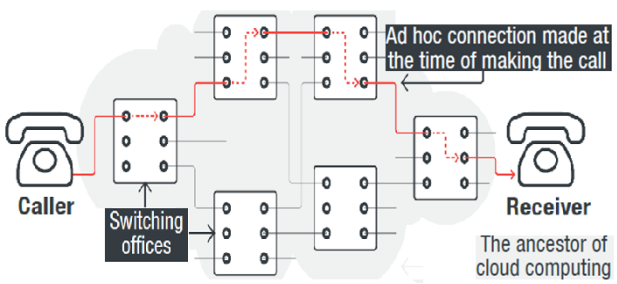

Fig. 1. Switch paths establishing voice circuits to carry voice calls in a circuit-switched network [4].

The Hardware Defined Network – Packet Switching. When the resource constraints and scalability limitations of circuit-switched networks became obvious, the emerging "new" information technology and circuit miniaturization became very attractive. Many carriers are on track to become content delivery networks (voice and video), replacing most methods people use to consume media content (Fig. 2).

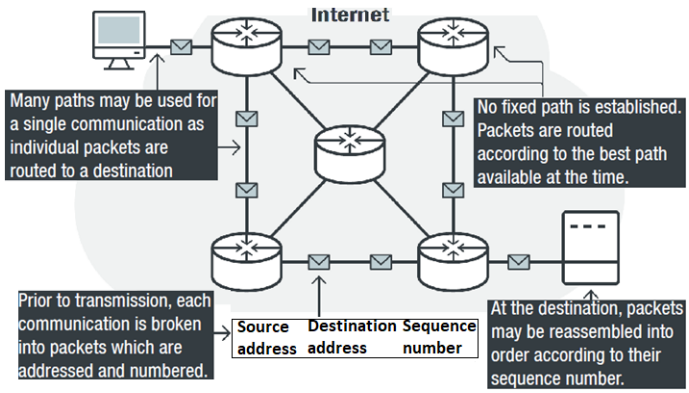

Fig. 2. Internet equipment responsible for establishing voice circuits to carry voice calls [4].

Packet-switched networks combine many of the vulnerabilities and risks in circuit-switched networks (e.g., wiretap, roaming frauds, SIM card supply chain issues, etc.) with "traditional" IT security risks (e.g., hackers, spies, viruses, worms, etc.). The primary approach of protecting these networks comes from an unscalable kind of network isolation in which every carrier attempts to replicate the IT security means.

The Software-Defined Network. The newer types of telecom automation require advanced management techniques called cloud orchestration or orchestrators, which include Software-Defined Network and Network Function Virtualization. These orchestrators handle the various hybrid circuit-like, packet-like networks called network slices. Such type of network architecture is extremely sophisticated. Note that each User Equipment has up to eight channels having different QoS features (up to eight QoS Flows) that transmit these flows through up to eight slices. The 5G architecture expects the underlying networks and base stations to ensure the required QoS characteristics (such as packet delay, packet loss) without specifying how (at least, by now).

Since these networks inherit the vulnerabilities of both circuit-switched and packet-switched networks, the result is that the effects of old risks will be amplified due to the automation of their delivery media (the carrier amplifies the effect of the attack), or new hybrid attacks will become available (telecom fraud viruses and worms).

Fraud Case 1: International Revenue Share Fraud. IRSF is a general term for a number of frauds. Generically, the frauds in this group are characterised by the involvement of three parties:

- One victim from whom fraudulent billing or criminal revenue is taken through a variety of methods, and two sets of criminals;

- Being the “grey or white” money laundering function group for stolen billing or revenue;
- Being a “black” function driving the hacking originating the fraud (Fig. 3).

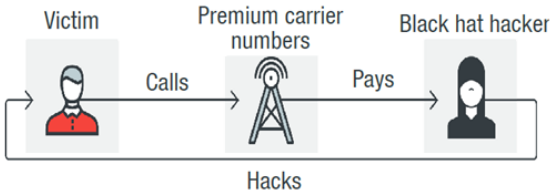

Fig. 3. The simplest IRSF scheme [4].

Fraud Case 2: Intermarket/Interconnect Bypass Fraud. SIM boxes are devices capable of using many SIMs at once. A SIM box can be used for making calls, originating data, or sending SMS (Fig. 4). When used to perform a criminal activity, this device and its management are controlled by the criminal and it passes only the information the criminal intends. According to a rough estimate, fraudsters can easily generate over US$100 per modem in a SIM box, and since one SIM box can contain 30 to 60 modems, this adds up to a US$6,000 revenue loss per day or over US$2 million per year.

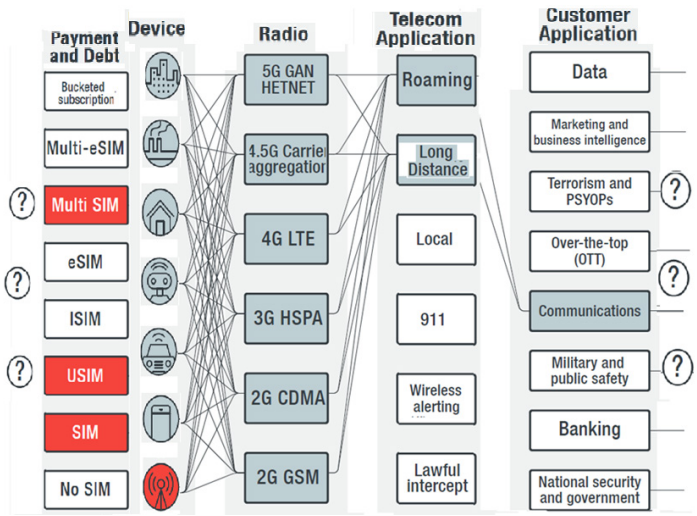

Fig. 4. Intermarket/interconnect bypass fraud threat model:
combined network model showing both ends of the telecom delivery “pipe”
at far-left and far-right ends of the diagram, each represented as ? sign [4].

In conclusion, on the one hand, the current trend indicates larger and more scalable attacks; on the other, additional motivators drawing attention to this class of attack are the very lucrative employment opportunities for individuals with security/hacking/fraud skills. At the time of writing [4], a senior individual might be offered US$250,000 and additionally US$150,000 in bonuses and equity, for a total of US$400,000 in salary. In Europe, a consultant might be offered 2,000 euros daily.

3. CYBERSECURITY IN MILITARY COMMUNICATIONS

The telecom modernisation process of the Department of Defence (DoD) through three generations:

- The implementation of signalling protocol SS7 and Advanced Intelligent Network;
- Transformation from SS7 to IP protocol;
- The extremely ambitious cybersecurity issues. During this process, the cyber vulnerabilities are increasing.

All these digital transformations asked for more and more skilled professionals in both telecommunications and software.

DoD cyber threats. According to a recent Government Accounting Office (GAO) report [6], the United States weapon systems developed between 2012 and 2017 have severe, even "mission critical" cyber vulnerabilities, and the federal information security needs to improve "the abilities to detect, respond to, and mitigate cyber incidents", increase its cyber workforce and cybersecurity training efforts. How to say for sure that all vulnerabilities are detected and removed?

DoD weapon systems are more software dependent and more networked than ever before (Fig. 5). From ships to aircraft, the weapons are becoming more technologically advanced and use more software and less hardware to control everything from navigation to weapon systems. The F-35 Lighting II software (aircraft) contains eight million lines of code and controls everything from flight controls to radar functionality, communications, and weapon deployment.

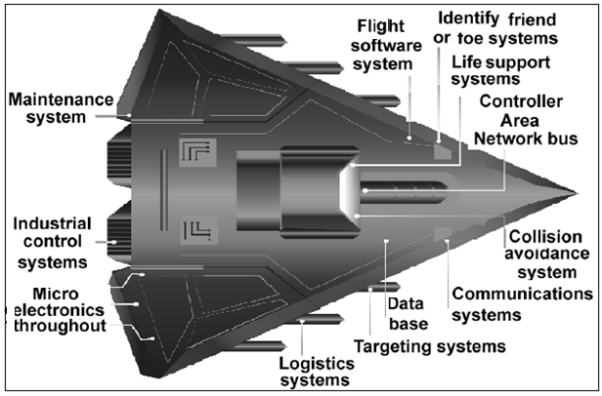

Fig. 5. Embedded software and information technology systems in weapon systems (represented via fictitious weapon system for classification reasons) [6].

DoD modernisation program. Under the pressure of the industry, the DoD is trying to introduce the latest achievements [7], namely, Software Defined Network and Network Function Virtualisation (Fig. 6), which, honestly speaking, increase cyber threats as any new technology added.

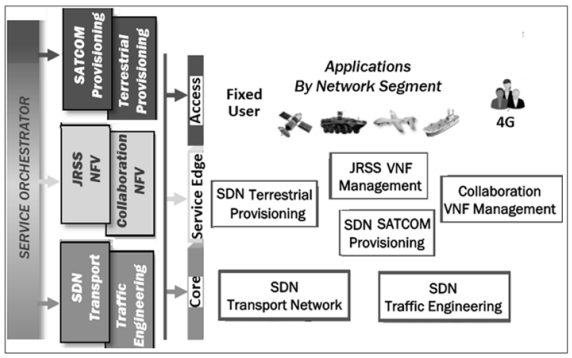

Fig. 6. The latest DISN architecture (the excerpt from slide 8 [7]).

The newly released cloud strategy of the Defence Department positions the general-purpose Joint Enterprise Defence Infrastructure (JEDI) cloud initiative as the foundation [8]. The strategy emphasises a cloud hierarchy at DoD, with JEDI on top. Fit-for-purpose clouds, which include MilCloud 2.0 run by the Defence Information Services Agency (DISA), will be secondary to the commercially run JEDI general-purpose cloud.

JEDI is not the first one into cloud computing. The Pentagon already is a multi-cloud environment. There are some 500 clouds in operation across DoD various offices, agencies and departments. Some of these are quite long and involve expenditures of billions of dollars. One of the largest is the milCloud managed by the DISA.

On 25 October 2019, the Pentagon awarded Microsoft a $10 billion cloud computing contract for 10 years bidding for the huge project JEDI, pitted leading tech titans Microsoft, Amazon, Oracle and IBM against one another. A key technological difficulty for the JEDI project is interoperability of clouds (Fig. 7). The interoperability of a technology (getting different parts to function in combination) can be divided into three main categories: internal, external, and iterative. Unfortunately, in each category, the Pentagon's JEDI cloud strategy leaves a series of unanswered questions that could spell disaster in the future [9].

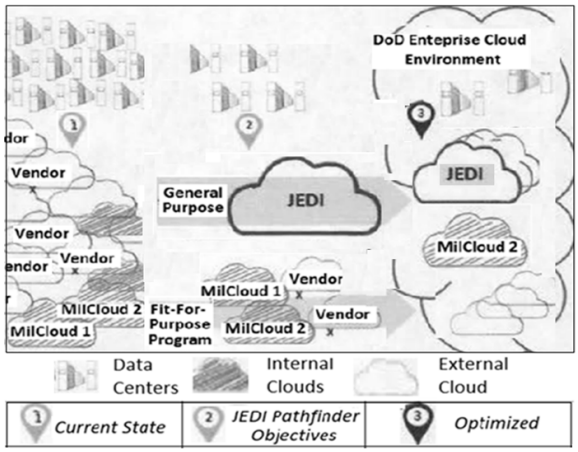

Fig. 7. DoD pathfinder to hybrid cloud environments and multiple vendors [10].

The Defence Innovation Unit (DIU) is a DoD organisation launched in 2015. The Joint Artificial Intelligence Centre is a focal point of the DoD AI Strategy [10]. The DoD has created this DoD Cloud Strategy to align with larger DoD cyber strategy, strengthening the security and resilience of the networks and systems that contribute to the Department's military advantage. Underscoring the potential magnitude of AI impact on the whole of society, and the urgency of this emerging technology race in the world, President Trump signed the executive order "Maintaining American Leadership in Artificial Intelligence" on 11 February 2019, launching the American AI Initiative. This was immediately followed by the release of DoD's first-ever AI strategy [11].

Some Criticism against Software-Defined Networking [12]. SDN does not solve any practical problems. All it does is taking the control plane of the network and centralising it. Due to redundancy, you cannot really just centralise it, you have to have multiple redundant control planes. This adds complexity. Controllers now have to control elements, implying a new control interface. This is more complex. Controllers are a security risk. The communication between the controller and element is a security risk. SDN causes every network operator become also a systems integrator: they now have to find a controller, controller software, and elements that interoperate. There is more complexity and much more work at a time when most enterprises would like to simplify their network operations and outsource them.

Some Criticism against Artificial Intelligence. Paper [13] presents a literature review of Machine Learning (ML) and Deep Learning (DL) methods for network security. The paper, which has mostly focused on the past three years, introduces the latest applications of ML and DL in the field of intrusion detection. Unfortunately, the most effective method of intrusion detection has not yet been established. Each approach to implementing an intrusion detection system has its own advantages and disadvantages. Thus, it is difficult to choose a particular method to implement an intrusion detection system over the others.

Datasets for network intrusion detection are very important for training and testing systems. The ML and DL methods do not work without representative data, and obtaining such a dataset is difficult and time-consuming. However, there are many problems with the existing public dataset, such as uneven data, outdated content and the like. These problems have largely limited the development of research in this area.

As AI programs become more sophisticated, the security measures designed to deal with them will also become more complex. AI is making the telecoms industry more efficient, but it comes at a cost of security.

DRSN are still ISDN based. No reason to be surprised that due to cyber threats the Defence Red Switch Network (DRSN) uses a 40 year-old ISDN technology. DRSN is a dedicated telephone network, which provides global secure communication services for the command and control structure of the United States Armed Forces (Fig. 8). The network is maintained by DISA and is secured for communications up to the level of Top Secret.

Fig. 8. Scheme of the government network DRSN and "Red phone".

4. CONCLUSIONS: WHAT TO TEACH TELECOMMUNICATIONS ENGINEERS?

When multibillion-dollar losses of fraud due to the vulnerabilities of 5G are coming, the need to work together for the benefit of all will have never been greater.

The main goal of the paper is to look for new university courses with regard to the digital economy [14]. The national programme "Digital Economy of the Russian Federation" names the main end-to-end digital technologies: Big Data; neuro-technologies and artificial intelligence; quantum technologies; industrial internet; robotics and sensory; wireless communication; technologies of the virtual and complemented realities and few others. Now it is time to revise our previous course list [15]. The same relates to cyber-security issues [16].

According to the latest Pentagon activities, the key attention in the field of Information Systems has been devoted to Cloud Strategy and Artificial intelligence. This Pentagon's new strategy has been developed after the serious critics of the current state recovered by GAO inspections. Due to the mentioned SDN and NFV criticism, it is reasonable to develop new education courses aimed at telecommunications engineers with the strong component of system approach, which gives the common view regarding all these latest technologies at the same time keeping in mind cyber security issues.

REFERENCES

1. Miladinovic, I., Schefer-Wenzl, S., & Hirner, H. (2019). Curriculum of a Telecommunications Study Program—A Matter of Trends? In *Proc. CONTEL2019. The 15th International Conference on Telecommunications*, 3–5 July 2019, Graz, Austria.
2. Global Telecom Crime Undermining Internet Security: Cyber-Telecom Crime Report. (21 March 2019). Available at https://www.trendmicro.com/vinfo/us/security/news/internet-of-things/global-telecom-crime-undermining-internet-security-cyber-telecom-crime-report
3. ThreatMetrix. (15 January 2019). *Telco Fraud: Why this Industry is Unique in the Cybercrime Landscape*. Available at https://www.threatmetrix.com/digital-identity-blog/cybercrime/telco-fraud-why-industry-unique-cybercrime-landscape/

4. Europol's European Cybercrime Centre. (21 March 2019). *Cyber-Telecom Crime Report 2019*. Available at https://www.europol.europa.eu/publications-documents/cyber-telecom-crime-report-2019
5. ETSI TS 123 501 V15.2.0. (2018-06). *5G; System Architecture for the 5G System* (Release 15). Available at https://www.etsi.org/deliver/etsi_ts/123500_123599/123501/15.02.00_60/ts_123501v150200p.pdf
6. United States Government Accountability Office. (9 October 2018). *GAO-19-128. Weapon Systems Cybersecurity. DOD Just Beginning to Grapple with Scale of Vulnerabilities. Report to the Committee on Armed Services*. Available at https://www.gao.gov/products/GAO-19-128
7. Osborn, Ch. (16 May 2018). *Defense Information Systems Network (DISN). An Essential Weapon for the Nation's Defense*. Available at file:///G:/Pentagon-book+/Osborn_%20DISN%20An%20Essential%20Weapon2018.pdf/
8. Williams, L.C. (5 February 2019). *DOD Cloud Strategy Puts JEDI at the Center*. Available at https://defensesystems.com/articles/2019/02/06/dod-cloud-strategy.aspx/
9. Keelan, T. (21 March 2019). *The Pentagon's JEDI Cloud Strategy is Ambitious, but Can it Work?*. Available at https://www.c4isrnet.com/opinion/2019/03/21/the-pentagons-jedi-cloud-strategy-is-ambitious-but-can-it-work/
10. Department of Defense. (December 2018). *DoD Cloud Strategy Readiness for Artificial Intelligence (Al)*.Available at https://media.defense.gov/2019/Feb/04/2002085866/-1/-1/1/DOD-CLOUD-STRATEGY.PDF
11. U.S. Department of Defense. (12 February 2019). *Summary of the 2018 Department of Defense Artificial Intelligence Strategy: Harnessing AI to Advance Our Security and Prosperity*. Available at https://media.defense.gov/2019/Feb/12/2002088963/-1/-1/1/SUMMARY-OF-DOD-AI-STRATEGY.PDF/
12. Li, T. (7 October 2015). *What are Some Criticisms, if any, against Software-Defined Networking?* Available at https://www.quora.com/What-are-some-criticisms-if-any-against-software-defined-networking
13. Xin, Y., Kong, L., Liu, Z., Chen, Y., Li, Y., Zhu, H., … & Wang, C. (2018). Machine Learning and Deep Learning Methods for Cybersecurity. *IEEE Access*, 35365–35381. DOI 10.1109/ACCESS.2018.2836950
14. Digital Economy of the Russian Federation. Order of the Government of the Russian Federation of 28 July 2017 No. 1632-p (Tsifrovaya ekonomika Rossiyskoy Federatsii. Rasporyazheniye Pravitel'stva RF ot 28.07.2017 N 1632-r). Available at http://ac.gov.ru/en/projects/014097.html
15. Namiot, D., & Sneps-Sneppe, M. (2017). On Internet of Things and Big Data in University Courses. *International Journal of Embedded and Real-Time Communication Systems*, *8* (1), 18–30.
16. Sneps-Sneppe, M., Sukhomlin, V., & Namiot, D. (2018). On Cyber-Security of Information Systems. In *Proc. Distributed Computer and Communication Networks. 21st International Conference, DCCN 2018* (pp. 201–211), 17–21 September 2018, Moscow, Russia.

INFORMĀCIJAS SISTĒMU KIBERDROŠĪBA UN TELEKOMMUNIKĀCIJU INŽENIERU APMĀCĪBA

M. Šneps-Šneppe, D. Namiots, R. Pauliks

K o p s a v i l k u m s

Rakstā apspriesti telekomunikāciju inženieru apmācības jautājumi. Telekomunikāciju risinājumu arhitektūra mainās ļoti ātri. Acīmredzot ir jāmaina arī apmācības programmas. Viens no galvenajiem pārmaiņu virzītājspēkiem telekomunikāciju risinājumos un apmācības programmās ir kiberdrošības jautājumi. Kiberdrošības jautājumi ir kļuvuši par galvenajiem jautājumiem visos procesos, kas saistīti ar digitālo pārveidi. Tajā pašā laikā ir skaidrs, ka izglītības attīstība telekomunikāciju jomā atpaliek no mūsdienu prasībām. Šie jautājumi izvirzās priekšplānā saistībā ar digitālās ekonomikas attīstību. Atsevišķi tiek apspriesti kiberdrošības jautājumi militāro telekomunikāciju jomā.

Atslēgas vārdi: *izglītība, kiberdrošība, telekomunikācijas*

sciendo

LATVIAN JOURNAL OF PHYSICS
AND TECHNICAL SCIENCES
2020, N 1-2

DOI: 10.2478/lpts-2020-0008

THE JOINT SLR (OPTICAL RANGE) AND RADAR-VLBI SATELLITE OBSERVATIONS USING VIRAC RADIO TELESCOPE RT32, RT16 AND SLR STATION RIGA

K. Skirmante[1]*, N. Jekabsons[1, 2], K. Salmins[3],
V. Bezrukovs[1], M. Nechaeva[4]

[1] Engineering Research Institute
"Ventspils International Radio Astronomy Centre",
Ventspils University of Applied Sciences,
101 Inzenieru Str., Ventspils, LV-3601, LATVIA
[2] Department of Physics and Mathematics, University of Latvia,
19 Raina Blvd., Riga, LV-1586, LATVIA
[3] Institute of Astronomy, University of Latvia,
19 Raina Blvd., Riga, LV-1586, LATVIA
[4] Moscow Power Engineering Institute (OKB MEI),
14 Krasnokazarmennaya Str., Moscow, 111250, RUSSIA
*e-mail: karina.krinkele@venta.lv

Joint VLBI and SLR satellite tracking is a novel tracking approach to explore potential applications and to work out common procedures to coordinate observations between astronomical observatories in Latvia. Global Navigation Satellite System (GNSS) satellites equipped with laser retroreflectors have been chosen as test targets because they are accessible by both measuring techniques – satellite laser ranging (SLR) and Very Long Base Interferometry (VLBI).

The first Joint SLR and VLBI observations of selected GNSS satellites using three of Latvian large-scale astronomical utilities – VIRAC radio telescopes RT32 and RT16 (Ventspils International Radio Astronomy Centre of Ventspils University of Applied Sciences) with L band receivers and SLR station Riga (Institute of Astronomy of University of Latvia) were obtained in 2016 (NKA16) and 2017 (NKA41 and NKA42).

Keywords: *VLBI, SLR, Joint observations, GNSS satellites*

1. INTRODUCTION

Satellite Laser Ranging (SLR) is a method of measuring distances to the satellites using very short laser pulses. At the SLR station, a very short laser pulse is generated, transmitted to the satellite, and reflected back to the station, where it is detected. A high precision event timer – using time and standard frequency derived from a specially dedicated GPS receiver or from primary time standard like caesium clock or hydrogen maser – measures the time of flight of the laser pulse with a precision of about 3 ps. Using the known velocity of light, one can thus determine the distance to the satellites – from a few hundred km up to more than 20,000 km – with subcentimeter accuracy.

The method of Very Long Baseline Interferometry (VLBI), one of the most powerful approaches used in radio astronomy, allows obtaining accurate determination of coordinates of radio sources. Since the 1980s, VLBI method is successfully applied for angular coordinate determination of artificial Earth satellites and interplanetary space stations with the precision 0.01–0.03 arcsec in single measurements. Since neither distance nor radial velocity of the object can be measured with VLBI method alone, it solves the navigation task only partly. These parameters can be obtained with space navigation methods (passive radar) or active radar. The combination of both radar methods can be used as radar-VLBI method. The space navigation methods apply the ranging and Doppler measurements using the on-board transmitters.

A radar VLBI method has been used for the refinement of the orbit parameters of space debris fragments, near-Earth asteroids and evaluation of rotation of planets [5]. It supplements the traditional radar methods with the interferometric reception of a ground-based transmitter signal reflected from the object [3]. Such an addition allows for measurements of distances, as well as for radial velocity, angle and angular velocity of the object. By the exploitation of several distant receiver stations of reflected radar signal, the radar VLBI has a potential for very high accuracy. In theory, the radar VLBI may yield all the motion parameters required for the formulation of a Newtonian orbital solution in a single measurement.

Since 2001, a large number of experiments on radar VLBI of objects in the near Earth space have been carried out with radio telescopes in Ukraine, Russia, Italy, China, Latvia, etc. [4]. One of such experiments was VLBI international experiment on radio location of the asteroid 2012 DA14 [1], which was organized on 15–16 February 2013 during its flyby close to the Earth. The aim of observations was to investigate and specify orbital parameters of the asteroid, as well as to evaluate its rotation period and some other characteristics. The asteroid was irradiated by the 5010.024 MHz frequency signal (radar RT-70, Evpatoria, Ukraine), whereas the echo signals were received by the radio telescopes RT-32 in Irbene (Ventspils, Latvia) and Medicina (Italy) in VLBI regime. A series of observations was implemented for different distances between the Earth and the asteroid (from 30000 km to 250000 km). The reflected signals were successfully received by the both VLBI-stations. Processing of the recorded signals allowed measuring the Doppler frequency and

interference frequency in order to improve the calculation of the radial and angular velocity of the asteroid. Processing and interpretation of the data were performed at Ventspils International Radio Astronomy Centre and Lobachevsky State University of Nizhny Novgorod, which was a collaboration partner of DA14 experiment.

2. GOAL OF THE COMBINATION OF VLBI AND SLR METHODS

The combination of SLR and VLBI is a novel approach; it is potentially reliable and accurate for large-scale NEO observations and space geodesy. Our long-term goal is to develop the methodology for potentially accurate and reliable measurements of all the coordinates and velocities in a few or even single observation(s). The aim of combining several optical and radar methods is mainly the reliability of the composite method. Radar methods (active and passive radar as well) yield an acceptable range and radial velocity resolution while VLBI allows for angle and angular rate information, these are all-weather measurements. SLR allows for instantaneous range measurements of centimetre or millimetre level precision; however, superior accuracy in the line of sight comes with constraints on weather conditions. Complementary SLR and radar-VLBI potentially give high precision tracking of space debris at the all deorbiting stages. An active spacecraft can be guided and real time traced with the mentioned method. In the future, combination of these technologies may serve as a basis for determination of ongoing dynamic processes on the Earth, maintenance of precise parameters of the coordinate system on the global scale and forecast of eventual risks and cataclysms in the future. Observation of critical or unique events in the near-Earth space is possible with the best available accuracy when methods are combined. Data processing from two independent simultaneous measurements (for example, with specific Kalman filters) may allow ruling out human errors or other sporadic error sources. Thus, reliability of overall measurement can be improved considerably even if actual accuracy is dictated by more accurate instruments (SLR).

3. EXPERIMENTAL PART

SLR and passive radar-VLBI observations of transmitting geodetic satellites (GPS and GLONASS) were carried out in 2016 and 2017. The aim of the observations was to develop the technology by means of accurate measurements of the deviations in orbital parameters of the known satellites. Two different technologies – SLR and VLBI – were combined, and simultaneous observations took place at the same time on the same objects. Thus, in 2016 SLR station in Riga and three VLBI stations (radio telescopes RT-16 and RT-32 in VIRAC of VUC and UNN (RT2) in NIRFI) were used in NKA16 experiments and more than 25 GPS and GLONASS satellites were tracked. On 23–24 September 2017, SLR station Riga and both VIRAC radio telescopes were used in NKA41 and NKA42 experiments. The example of NKA41 observation schedule plan is shown in Table 1.

Table 1

NKA41 Observation Schedule Plan

Start time of scan (UTC)	End time of scan (UTC)	Observed object	Sky frequency, MHz
17:45	17:55	CASA	1602.5625
18:00	18:30	Cosmos 36111/ Glonass 116	1602.5625
18:35	18:40	CASA	1575
18:45	19:15	Galileo 40890 / Galileo 206	1575
19:20	19:25	CYGNUSA	1602
19:30	20:10	Cosmos 41554 / Glonass 136	1602
20:05	20:10	CYGNUSA	1599.75
20:15	20:45	Cosmos 39155/ Glonass 131	1599.75
20:50	20:55	CYGNUSA	1602.5625
21:00	21:30	Cosmos 36111/ Glonass 116	1602.5625
21:35	21:40	3C123	1599.75
21:45	22:15	Cosmos 39155/ Glonass 131	1599.75
22:20	22:25	3C123	1602
22:30	23:00	Cosmos 41554/ Glonass 136	1602
23:05	23:10	3C123	1575
23:15	23:45	Galileo 40890/ Galileo 206	1575
23:50	23:55	3C123	1575

Observation and Data Processing in RT32 and RT16 Sites

The L band receivers were used in both stations and data were recorded with 8 MHz bandwidth and LCP (Left Circular Polarization) in VDIF formats using FlexBuff (at RT32) and Mark5 (at RT16) recorders.

3C123, CASA, CYGNUSA objects were included in the schedule for radio telescopes RT32 and RT16 calibration purpose only. Each scan of observation was divided into two parts – with duration of 14 min and 15 min each.

The data processing was carried out using KANA correlator (developed in VIRAC). KANA was designed as a software correlator (ANSI C programming language with POSIX compatibility). Text files in JSON (JavaScript Object Notation) format were used for parametric control of the correlator routines. As for observation data, KANA could process NRFI, and MARK5 a, b data formats. The reader of more recent VDIF data format was added to KANA with the aim of data processing during NKA experiments in 2016.

Satellite laser ranging schedule usually gives tracking priorities according to ILRS settings for a particular time period. In this case, the GNSS satellites of Ventspils list were given higher priority. To obtain a valid measurement, at least three to five normal points are required. Each normal point or compressed range for GNSS satellites takes five minutes to complete. The data processing was performed according to the ILRS standard procedures. The obtained results are provided in Table 2.

Table 2

The Results of Data Processing in SLR Station Riga Site

Satellite	Start	Stop	Track time (sec)	Number of normal points	Normal point RMS (ps)	Overlap with VLBI (%)
glonass116	9/23/2017 20:31	9/23/2017 21:21	2449.7	9	90.66	100
glonass131	9/23/2017 21:40	9/23/2017 22:15	2008.1	8	180.66	100
glonass136	9/23/2017 22:35	9/23/2017 22:45	502.1	3	25.9	40
galileo205	9/24/2017 19:22	9/24/2017 19:29	145.2	2	27	100
glonass136	9/24/2017 19:04	9/24/2017 19:45	2439	7	118.53	40
glonass131	9/24/2017 20:20	9/24/2017 20:39	810.7	4	143.35	100
glonass107	9/24/2017 22:35	9/24/2017 23:29	2912.5	7	98.14	0
glonass102	9/25/2017 1:47	9/25/2017 2:11	1336.2	5	71.98	0
galileo206	9/25/2017 2:52	9/25/2017 3:01	286.3	2	241.15	0

During two consecutive nights, there were four sets obtained, which at least partially overlapped with VLBI sessions. Table 3 shows the obtained SLR normal point precision estimates with respect to GNSS orbits as given by GOVUS online tools from Wrozlaw University [7].

Table 3

The Obtained SLR Normal Point Precision Estimates with Respect to GNSS Orbits

Normal point date/time	Satellite	sat_ prn	residual (mm)
9/23/2017 20:37	Glonass-136	R11	-1.4
9/23/2017 20:43	Glonass-136	R11	-10
9/23/2017 20:46	Glonass-136	R11	11.3
9/23/2017 19:41	Glonass-131	R02	-15.2
9/23/2017 19:48	Glonass-131	R02	-76.3
9/23/2017 19:52	Glonass-131	R02	-19.1
9/23/2017 19:59	Glonass-131	R02	-9.1
9/23/2017 20:03	Glonass-131	R02	-9.9
9/23/2017 20:08	Glonass-131	R02	-29.6
9/23/2017 20:12	Glonass-131	R02	-11.6
9/23/2017 20:15	Glonass-131	R02	40.4
9/23/2017 18:34	Glonass-116	R01	-42.5
9/23/2017 18:36	Glonass-116	R01	-1.4
9/23/2017 18:42	Glonass-116	R01	-36.2
9/23/2017 18:47	Glonass-116	R01	-15.9
9/23/2017 18:54	Glonass-116	R01	-18.3
9/23/2017 18:59	Glonass-116	R01	-44.5
9/23/2017 19:00	Glonass-116	R01	-17.3
9/23/2017 19:07	Glonass-116	R01	35.5
9/23/2017 19:14	Glonass-116	R01	-75.1
9/24/2017 18:24	Glonass-131	R02	-53
9/24/2017 18:27	Glonass-131	R02	-21.3
9/24/2017 18:33	Glonass-131	R02	-29.1
9/24/2017 18:37	Glonass-131	R02	-59.4
9/24/2017 17:04	Glonass-136	R11	-24.1
9/24/2017 17:07	Glonass-136	R11	-22.1
9/24/2017 17:12	Glonass-136	R11	-27.3
9/24/2017 17:34	Glonass-136	R11	-19
9/24/2017 17:38	Glonass-136	R11	-25.7
9/24/2017 17:43	Glonass-136	R11	-5.1
9/24/2017 17:45	Glonass-136	R11	-12.5
9/24/2017 17:23	Galileo-205	E24	46.2
9/24/2017 17:25	Galileo-205	E24	-15.5
9/24/2017 20:37	Glonass-107	R13	8.2
9/24/2017 20:42	Glonass-107	R13	-29.3
9/24/2017 20:46	Glonass-107	R13	-0.3
9/24/2017 20:52	Glonass-107	R13	-22.8
9/24/2017 20:55	Glonass-107	R13	-15
9/24/2017 21:24	Glonass-107	R13	5.2
9/24/2017 21:26	Glonass-107	R13	1.9
9/24/2017 23:49	Glonass-102	R15	-38.9
9/24/2017 23:52	Glonass-102	R15	-29.6
9/24/2017 23:55	Glonass-102	R15	-26.8
9/25/2017 00:07	Glonass-102	R15	-36.8
9/25/2017 00:11	Glonass-102	R15	-68.6
9/25/2017 00:56	Galileo-206	E30	79.3
9/25/2017 01:01	Galileo-206	E30	902.4

4. CONCLUSIONS

Work by joint tracking procedure implementation using SLR and VLBI technologies was started in 2016 to organise NKA16 (2016), NKA41 and NKA42 (2017) observations using VIRAC radio telescopes RT32 and RT16 and SLR station Riga. Unfortunately, NKA16 (2016) experiment was not successful due to technical issues of RT16 and RT32 related to clock synchronization and registration technologies and due to unsuitable weather conditions (rain and fog) for SLR station. NKA41 and NKA42 (both implemented in 2017) experiments were successfully organised and managed for both VIRAC radio telescopes RT32 and RT16 and SLR station Riga. In NKA41 experiment, all of the satellites were successfully observed by RT32 and RT16 and three of the four satellites were successfully observed by SLR station Riga. In NKA42 experiment, all satellites were observed in all included

stations. It gives a great probability to verify results from data processing of both methods – SLR and radar VLBI, respectively.

Potential applications for joint SLR and VLBI observations were identified. Chinese Atmospheric density detection and Precise Orbit Determination (APOD) satellite tracking could be done using joint SLR and VLBI observation. VLBI radio telescopes can be used in an ideal fashion to link the dynamic reference frames of the satellite with terrestrial and, most importantly, to the celestial reference frame as defined by the positions of quasars [6]. Triggered measurements will be performed using joint optical and radar tracking. The main idea of these measurements is a rapid reaction on the near-Earth space to unexpected events such as satellite collisions, identification of unexpected celestial body, etc. It is possible to develop a limited rapid triggered response capability of the combined SLR-VLBI methodology, including protocol and software development for this purpose. Several space geodesy applications can be developed using the results of the joint SLR and VLBI observations.

Possibilities of further research areas of complementary SLR and radar-VLBI methods: establishing data formats, uniform NEO trajectory description, pointing software, common protocol and session schedule generation, data processing method development, including Kalman type filters, resolution of spatial directions. There are possibilities to develop the mobile VLBI station. Design of the mobile VLBI station will be based on the existing design of ionosphere receiver already developed by the team and deployed on VIRAC RT-32. Single beam-parking mode of operation is specified for the mobile station (no tracking). Live correlation of radar VLBI data (reVLBI) could be developed and implemented in complementary SLR and radar-VLBI system.

ACKNOWLEDGEMENTS

The present research has partially been supported by the National Research Programme of Latvia (project "Multifunctional Materials and Composites, Photonics and Nanotechnology (IMIS2)"; sub-project No. 1.4 "Preparation of the Instrument of Near Earth Object Observation for Safe Cosmic Space Ensuring").

REFERENCES

1. Nechaeva, M., Antipenko, A., Bezrukov, D., Bezrukovs, Vl., Dementjev, A., Dugin, N., … & Voytyuk, V. (2013). First Results of the VLBI Experiment on Radar Location of the Asteroid 2012 DA14. *Baltic Astronomy*, *22*, 341–346.
2. Bezrukovs, Vl., Bleiders, M., Orbidans, A., & Bezrukovs, D. (2016). Broadband Receiving Systems for 4.5–8.8 Ghz Radio Astronomical Observations at Irbene Radio Telescopes RT32 and RT16. *Space Research Review, 4*, 62–76. ISBN 978-9984-48-053-7
3. Molotov, I.E., Volvach, A.E., Konovalenko, A.A., Falkovich, I.S., Litvinenko, L.N., Negoda, A.A., … & Liu, X. (2004). International Experiments on Development of VLBI Radar Method for Research of Near-Earth Bodies. *Kosmichna Nauka i Tekhnologiya, 10* (2/3), 87–92.

4. Molotov, I., Nechaeva, M., Falkovich, I., Konovalenko, A., Agapov, Vr., Tuccari, G., … & Bezrukov, D. (2008). Astrometry of the Solar System Bodies with VLBI Radar. In *the 5th General Meeting of the International VLBI Service for Geodesy and Astrometry. Measuring the Future* (pp. 9–10), 2–6 March 2008, St. Petersburg, Russia. ISBN 978-5-02-025332-2
5. Molotov, I., Konovalenko, A., Agapov, V., Sochilina, A., Lipatov, B., Molotov, E., & Gorshenkov, Y. (2002). Detection of Space Debris with VLBI Radar Technique. In *34th COSPAR Scientific Assembly, the Second World Space Congress,* 10–19 October 2002, Houston, TX, USA.
6. Tang, G., Sun, J., Li, X., Liu, S., Chen, G., Ren, T., & Wang, G. (2016). APOD Mission Status and Observations by VLBI. In *International VLBI Service for Geodesy and Astrometry 2016 General Meeting Proceedings: "New Horizons with VGOS"* (pp. 363–367).
7. Zajdel, R., Sosnica, K., & Bury, G. (2017). A New Online Service for the Validation of Multi-GNSS Orbits Using SLR. *Remote Sens., 9* (10), 1049. https://doi.org/10.3390/rs9101049
8. International Laser Ranging Service. (n.d.). *CRD Format Overview, Version V1.01*. Available at https://ilrs.cddis.eosdis.nasa.gov/data_and_products/formats/crd.html

APVIENOTIE SLR (OPTISKĀ DIAPAZONA) UN RADARA VLBI (RADIO DIAPAZONA) SATELĪTU NOVĒROJUMI, IZMANTOJOT VSRC RADIOTELESKOPUS RT32 UN RT16 UN SLR STACIJU RĪGA

K. Šķirmante, N. Jēkabsons, K. Salmiņš,
Vl. Bezrukovs, M. Nečaeva

K o p s a v i l k u m s

Divu astronomisku tehniku apvienojums – ļoti garas bāzes līnijas interferometriju (VLBI) un satelītu lāzerlokāciju (SLR) – ir jauna metode, lai veiktu satellītnovērošanu. Kopīgiem novērojumiem ir nepieciešams izstrādāt vienotas novērojumu procedūras, lai koordinētu novērojumus starp vairākām astronomiskajām novērošanas stacijām Latvijā.

Globālās navigācijas satelītu sistēmas (GNSS) satelīti, kas aprīkoti ar lāzeru atstarotājiem, tika izvēlēti kā noverojumu mērķavoti, jo tos var novērot ar abām novērojumu metodēm – SLR un VLBI.

2016. gadā (NKA41) un 2017. gadā (NKA16 un NKA42) tika veikti pirmie apvienotie SLR un VLBI novērojumi, novērojot izvēlētos GNSS satelītus un izmantojot trīs lielmēroga astronomiskos instrumentus – VSRC radioteleskopus RT32 un RT16 (Ventspils Augstskolas Inženierpētniecības institūts "Ventspils Starptautiskais radioastronomijas centrs") ar L-frekvenču joslas uztvērējiem un SLR staciju Rīga (Latvijas Universitātes Astronomijas institūts).

Atslēgas vārdi: *VLBI, SLR, vienotie novērojumi, GNSS satelīti*

sciendo

LATVIAN JOURNAL OF PHYSICS
AND TECHNICAL SCIENCES
2020, N 1-2

DOI: 10.2478/lpts-2020-0009

LAND COVER CLASSIFICATION USING VERY HIGH SPATIAL RESOLUTION REMOTE SENSING DATA AND DEEP LEARNING

R. Ķēniņš

Engineering Research Institute
"Ventspils International Radio Astronomy Centre",
Ventspils University of Applied Sciences,
101 Inzenieru Str., Ventspils, LV-3601, LATVIA
E-mail: roberts.kenins@venta.lv

The paper describes the process of training a convolutional neural network to segment land into its labelled land cover types such as grass, water, forest and buildings. This segmentation can promote automated updating of topographical maps since doing this manually is a time-consuming process, which is prone to human error. The aim of the study is to evaluate the application of U-net convolutional neural network for land cover classification using countrywide aerial data. U-net neural network architecture has initially been developed for use in biomedical image segmentation and it is one of the most widely used CNN architectures for image segmentation. Training data have been prepared using colour infrared images of Ventspils town and its digital surface model (DSM). Forest, buildings, water, roads and other land plots have been selected as classes, into which the image has been segmented. As a result, images have been segmented with an overall accuracy of 82.9 % with especially high average accuracy for the forest and water classes.

Keywords: *land cover classification, neural networks, remote sensing, topographic map*

1. INTRODUCTION

Nowadays the usage of convolutional neural networks for image recognition tasks and computer vision is widespread. Remote sensing data of the Latvian Geospatial Information Agency (LGIA) cover all of Latvia's territory and access to these data is free for public entities. Using these data, it is possible to prepare training images for a neural network, which can automatically predict land cover types and, therefore, the process of updating maps could be made easier.

The aim of the study is to evaluate the application of the U-net convolutional neural network for land cover classification using countrywide aerial data.

The methods have been applied to the test regions in the city of Ventspils using LGIA LIDAR data and orthophoto maps.

2. DATA SETS AND PREPARATION

Lidar, commonly spelled as LiDAR, is an acronym that stands for light detection and ranging – intense beams of light are emitted and the time it takes for the reflections to be detected by the sensor is measured. Using this information, it is possible to compute the distance to various objects. Lidar is similar to radar with the difference being that it is based on discrete pulses of laser light instead of radio waves [3].

Data used for neural network training:

- TIFF Format CIR (colour-infrared) map of Ventspils (25661x28636 resolution). Usually images consist of 3 colour bands – red, green and blue – this is called the RGB colour model and this kind of image is taken by most digital cameras. CIR images are taken by cameras, which can detect infrared light and, in this case, the red band is replaced by a near infrared band, green band – by red and green band – by blue.
- TIFF format Ventspils DTM map (6416x7159 resolution). Digital terrain model describes the natural land terrain height above sea level.
- TIFF format Ventspils DSM map (6416x7159 resolution). Digital surface model describes the land surface with all of its objects, e.g., building, trees. Figure 1 shows a visual comparison between these two models.

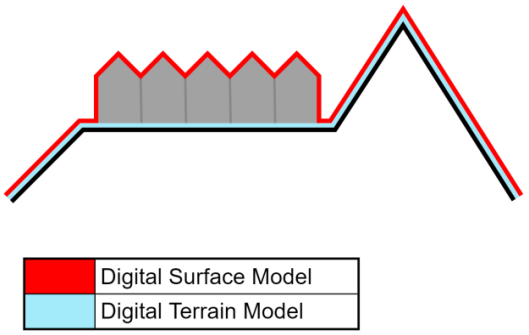

Fig. 1. Initial image, CNN filter and a resulting matrix [4].

3. NEURAL NETWORK ARCHITECTURES

A convolutional neural network (CNN) is a type of neural network that is used for image recognition and processing and it is specifically designed to process raster data. Convolutional neural networks get their name from the convolution operator. Convolution preserves the relationship between neighbouring pixels by learning image properties based on smaller squares of input data.

Relationships between neighbouring pixels are analysed using a filter. The filter size is user specified (usually 3x3 or 5x5) and the filter is “shifted” across the

image starting from the upper left corner to bottom right. A value that depends on the filter is calculated at each point in the image using the convolution operator.

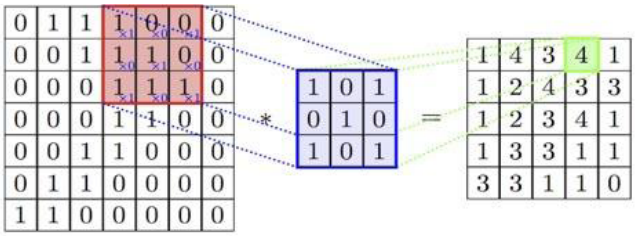

Fig. 2. Initial image, CNN filter and a resulting matrix [1].

After the filters have shifted across the image, a feature map is generated for each of them. Using this feature map and activation functions, it is determined whether the part of the picture contains the specific feature.

Convolutional neural networks consist of three layer types:

1. Convolution layer is the first layer to extract features from an input image. Convolution preserves the relationship between pixels by learning image features using small squares of input data.
2. Max-pooling layer – Max pooling takes the largest element from the rectified feature map. Taking the largest element could also take the average pooling. Sum of all elements in the feature map is called sum pooling.
3. Fully connected layer – the output is flattened and fed into this layer.

U-net is one of the most widely used CNN architectures for image classification tasks where it is necessary not only to determine the class of the whole image but also to segment the image into classes, creating masks that separate different classes within an image.

U-net was developed by Olaf Ronneberger for biomedical image segmentation. Some of the advantages U-net architecture provides are as follows:

1. Good results in various real-life tasks, especially in biomedicine. U-net has many uses in biomedical image segmentation, such as brain and liver image segmentation.
2. Network works relatively fast and is capable of segmenting a 512x512 image within less than a second.
3. Architecture is able to achieve considerable results even without a large training dataset.

U-net gets its name from the fact that the network architecture resembles the letter “U” [5], [6].

4. TRAINING PROCESS AND RESULTS

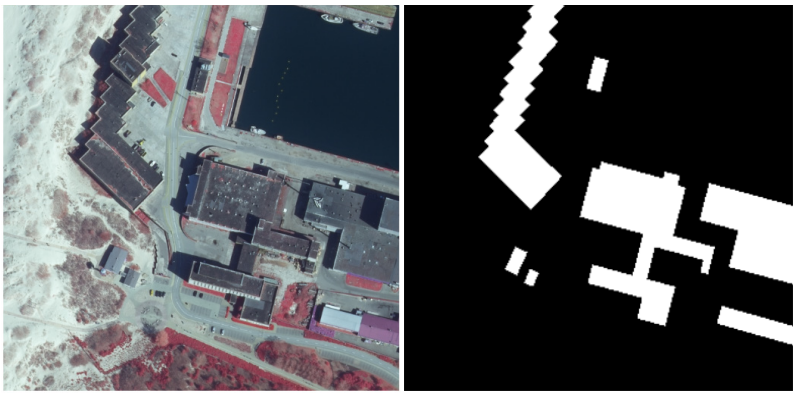

Fig. 3. CIR image and image showing only class "buildings".

Training set includes multiband images and respective labelled images showing class labels for each pixel. Multiband images for this study have been formed using 4 bands: NIR, red, green bands of CIR images and DSM. Labelled images have been obtained by rasterizing land cover information in the topographic map provided by LGIA. Neural network has been trained for 5 classes – roads, water, buildings, forest and other land plots because they are the most common land cover types in the training images. Since available GPU resources are limited, large resolution images have been split into smaller squares (160x160 pixels) and then used for training the neural network. The size of these squares is called patch size.

For the first experiment (see Fig. 5), training has been done with the following parameters set: epochs = 80, patch size = 96, batch size = 20, training images = 2000, and validation images = 500. The resulting image is a 3-channel RGB TIFF file and its resolution matches the image provided for prediction.

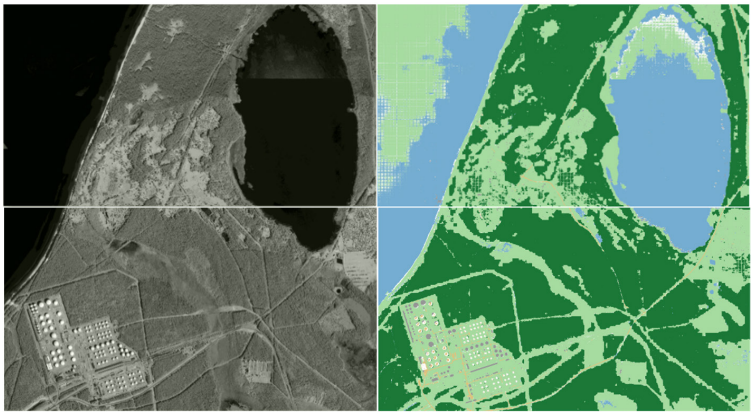

Fig. 4. The first band of the testing image and its land cover prediction.

The results seen in Fig. 5 have been obtained with the following parameters: epochs = 150, patch size = 160, batch size = 20, training images = 2000, and validation images = 500.

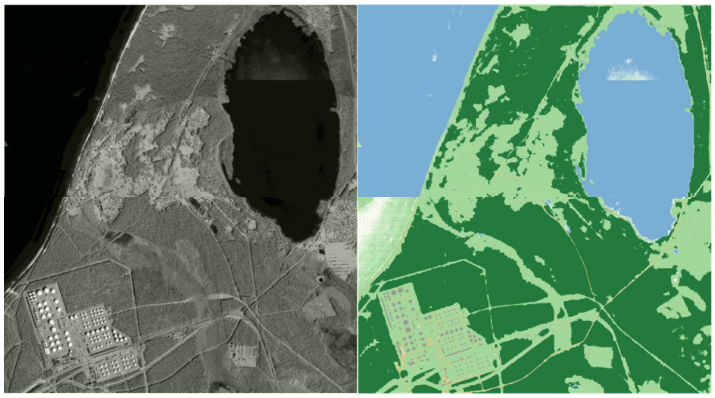

Fig. 5. Prediction with an increased epoch and data amount.

Accuracy has been calculated by creating a confusion matrix. The matrix is constructed by determining whether the predicted class matches the actual class using validation points. Over 1500 validation points arranged in a grid-like pattern have been selected in the independent test area in the northern part of Ventspils. As an example, some of the points can be seen in Fig. 6 and their respective confusion matrix is provided in Table 1. The largest number of validation points matches the forest and water land cover types.

Fig. 6. Example of validation points used to calculate accuracy.

Table 1

Confusion Matrix Based on the Example of Validation Points in Fig. 7

Forest		Actual class				
		Water	Roads	Buildings	Other	
Predicted class	Forest	722	0	3	0	25
	Water	0	234	0	1	3
	Roads	0	0	13	1	1
	Buildings	0	1	0	8	0
	Other	104	28	75	23	241

Table 2

Producer (PA) and User (UA) Accuracy by Land Cover Type

Land cover type	PA for the 1st attempt (%)	PA for the 2nd attempt (%)	UA for the 1st attempt (%)	UA for the 2nd attempt (%)
Forest	87.4	88.6	96.3	97.7
Water	89.0	94.3	98.7	100
Roads	14.3	16.1	86.7	93.7
Buildings	25.0	29.4	88.9	100
Other	89.3	91.6	51.2	45.0

As seen in Table 2, producer accuracy has increased by an average of 2 % between these 2 attempts. Producer accuracy has increased, whilst building accuracy and road producer accuracy are still the lowest when compared to other classes.

5. CONCLUSIONS

Using convolutional neural networks, it is possible to detect and classify land cover types for 5 classes with more than 80 % overall accuracy. Precision of the results is dependent on the selected neural network architecture, the amount of training data, epochs, resolution of training data, as well as the number of classes. It is possible to improve the precision of predictions by combining various remote sensing data, therefore increasing data amount.

On average, the highest classification accuracy has been achieved for the water and forest classes, which is possibly due to the fact that in nature these land cover types are less diverse and more similar to each other than roads or buildings. Therefore, fewer data are required to train the neural network. In order to achieve higher accuracy, a neural network should be trained and evaluated over vaster areas, and feature maps should be examined to study learned features.

REFERENCES

1. Chatterjee, S. (2017). *Different Kinds of Convolutional Filters.* Available at https://www.saama.com/blog/different-kinds-convolutional-filters/
2. Prabhu, R. (2018). Understanding of Convolutional Neural Network (CNN) – Deep Learning. Available at https://medium.com/@RaghavPrabhu/understanding-of-convolutional-neural-network-cnn-deep-learning-99760835f148
3. Carter, J., Schmid, K., Waters, K., Betzhold, L., Hadley, B., Mataosky, R., & Halleran, J. (2012). *Lidar 101: An Introduction to Lidar Technology, Data, and Applications*. National Oceanic and Atmospheric Administration (NOAA) Coastal Services Center, Charleston, South Carolina. Available at https://coast.noaa.gov/data/digitalcoast/pdf/lidar-101.pdf
4. Yodin. (2015). *Surfaces Represented by a Digital Surface Model and Digital Terrain Model*. Licensed under the Creative Commons Attribution-Share Alike 4.0 International license (https://creativecommons.org/licenses/by-sa/4.0/deed.en). Available at https://commons.wikimedia.org/wiki/File:DTM_DSM.svg

5. Lamba, H. (n.d.). *Understanding Semantic Segmentation with UNET.* Available at https://towardsdatascience.com/understanding-semantic-segmentation-with-unet-6be4f42d4b47
6. Ronneberger, O., Fischer, P., & Brox, T. (2015). *U-Net: Convolutional Networks for Biomedical Image Segmentation*. Available at https://arxiv.org/abs/1505.04597

ZEMES PĀRSEGUMU KLASIFIKĀCIJA, IZMANTOJOT ĻOTI AUGSTAS TELPISKĀS IZŠĶIRTSPĒJAS TĀLIZPĒTES DATUS UN DZIĻĀS APMĀCĪBAS NEIRONU TĪKLUS

R. Ķēniņš

K o p s a v i l k u m s

Šajā dokumentā tiek aprakstīts konvolūcijas neironu tīklu apmācības process zemes segmentācijas nolūkiem vairākās klasēs. Šīs klases ir zemes pārseguma veidi, piemēram, zāle, ūdens, mežs vai ēkas. Segmentācija nepieciešama topogrāfisko karšu sastādīšanai un manuāli šī uzdevuma veikšana ir laikietilpīgs kā arī, iespējams, kļūdains process. Lai paātrinātu un vienkāršotu karšu atjaunošanas procesu, var izveidot automatizētu risinājumu, izmantojot U-net neironu tīkla arhitektūru. Šī arhitektūra sākotnēji tika izstrādāta biomedicīnisko attēlu segmentācijai un tā ir viena no visplašāk izmantotajām CNN arhitektūrām. Apmācības dati tiek sagatavoti, izmantojot Ventspils pilsētas krāsu infrasarkanos attēlus un digitālo virsmas modeli. Mežs, ēkas, ūdens, ceļi un cita zeme tika atlasītās kā klases, kurās attēls tiek segmentēts. Rezultātā attēli tika segmentēti ar 82,9 % kopējo precizitāti, atsevišķām klasēm, kā mežam un ūdenim sasniegta vēl augstāka precizitāte.

Atslēgas vārdi: *neironu tīkli, tālizpēte, topogrāfiskā karte, zemes pārsegumu klasifikācija*

sciendo

LATVIAN JOURNAL OF PHYSICS
AND TECHNICAL SCIENCES
2020, N 1-2

DOI: 10.2478/lpts-2020-0010

GNSS RTK PERFORMANCE IMPROVEMENTS USING GALILEO SATELLITE SIGNAL

J. Zvirgzds[1]*, A. Celms[2]

[1]Latvian Geospatial Information Agency
43 O.Vaciesa Str., Riga, LV-1004, LATVIA
[2]Latvia University of Life Sciences and Technologies
2 Liela Str., Jelgava, LV-3001, LATVIA
*e-mail: janis.zvirgzds@lgia.gov.lv

Two factors of the existing GNSS Real-Time Kinematic (RTK) positioning are as follows: distance-dependence and unreliable ambiguity resolution under bad observation conditions in cities or forests. Use of multi-frequency GNSS signals and systems could possibly redefine RTK services in LatPos, regionally and globally, and more redundant measurements from multiple satellite systems, such as NAVSTAR, Galileo, Glonass and BeiDou, can improve the performance of RTK measurement results in terms of accuracy, availability, reliability and time to fix. The benefits of multiple systems of GNSS services are as follows: 1) savings in the reference station infrastructure costs, and 2) improvement on RTK preciseness and reliability for the professional users. The paper aims at studying how the RTK system, using multiple satellite constellations, performs, adding Galileo signal measurements. Galileo measurements are observed using a field receiver and corrections received from LatPos base station network. Numerical analysis is performed using real-time corrections in field receivers, and results from collected RINEX data are compared by various computing schemes, such as L1/L2 and wide lane signals, NAVSTAR and NAVSTAR with Galileo measurements. The results have preliminary demonstrated the significant improvement using both GNSS satellite signals. Further improvements on the LatPos system have been introduced and the planned improvements shown.

Keywords*: Galileo, global navigation satellite system, satellite signal*

1. INTRODUCTION

Real-Time Kinematic (RTK) measurements with centimetre accuracy are used in all areas of economy.

Surveying measurements are done in cities and wooden areas with poor visibility. More than 5 satellites are needed to proceed with RTK measurements.

If multiple signals from navigation systems can be received by the GNSS RTK equipment, then there is a chance that satellite signals at least from five satellites will be received. Multi-constellation and multi-frequency GNSS RTK is a complex real-time process that aims at providing cm-level positioning accuracy with as few as possible data epochs for variable user kinematics and even in difficult measuring environments. RTK performance characteristics need to be carefully selected to be able to evaluate the system and users could use services for all they need in their applications.

The receiver parameters are used in the article to assess the benefits of Galileo for RTK:

1. Satellite usage. Number of satellites used in RTK fixed solutions with an elevation cut-off angle of 15°.
2. Availability. RTK fixed positions in clear sky visibility.
3. Accuracy. Deviation differences of RTK fixed positions between two receivers – with Galileo signal reception and without Galileo system. Both receivers running simultaneously.
4. Reliability. Percentage that the position error (with respect to ground truth) is less than 3 x coordinate quality (CQ) indicator.
5. Time to Fix. Time needed to reach the RTK fixed solution after each instrument restart [1].

In Latvia, RTK correction provider is the Latvian Positioning System (LatPos) maintained by LGIA.

In the territory of Latvia, the State Land Service has started to develop a real-time correction system since 2005 by creating the Latvian positioning system – LatPos, which was based on GNSS available at that time. Since 2006, the Latvian Geospatial Information Agency has been responsible for maintenance and development of LatPos [2]. As a state geodetic system, LatPOS is maintained and developed on a regular basis, so the possibility is created to ensure coordinate precision real-time corrections anytime, anywhere for spatial measurements of different kind. Originally, it was planned to use LatPOS real-time correction system in surveying and geodesy for determination of precise coordinates in real time of the measurement. As GNSS technologies developed, their usage also improved in various other branches of economics.

Research is conducted using statistical methods, comparing different measurement conditions to display the contribution of the Galileo GNSS system on the improvement of measurement accuracy.

The change in the number of satellites can be compared to the planned number. Let us consider the situation on 23 July for GNSS systems. Measurements were taken in the open, providing complete satellite signal reception. The present article studies the increase in measurement accuracy and measurement stability using Galileo system signals. The number of satellites at observation time (Fig. 1) has been considered.

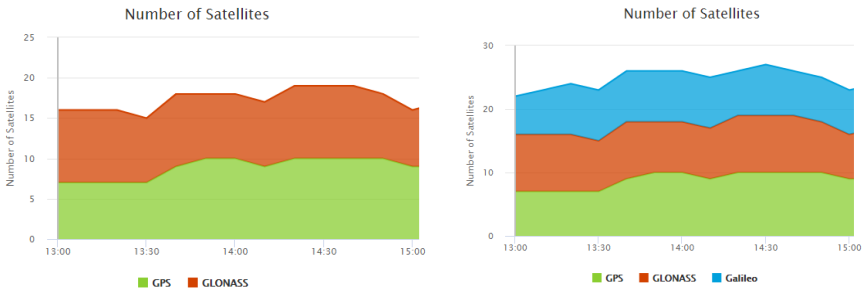

Fig. 1. Number of satellites in view (Trimble Online Planning).

Making measurements only with NAVSTAR and Glonass systems, the number of satellites is not more than 20 space vehicles. Adding Galileo GNSS signal, eight satellites will be added. It will significantly increase the number of available satellites.

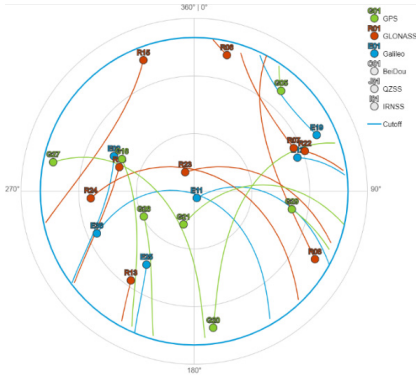

Fig. 2. Satellite sky plot.

As it can be observed (Fig. 2), Galileo satellites are in good constellation and this situation is proven by Position Dilution of Precision (PDOP), PDOP value of which (Fig. 3) must be near 1, then it is the best satellite constellation.

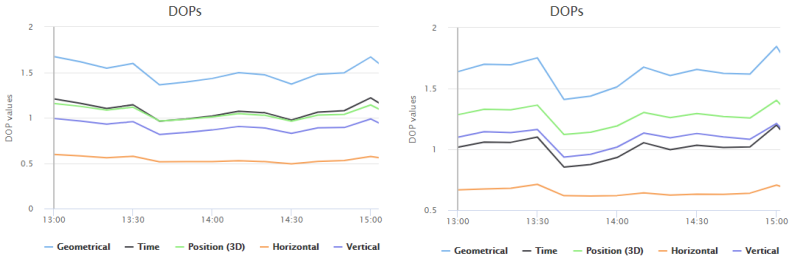

Fig. 3. Dilution of precision.

Without Galileo satellite signals, PDOP is 1.23, but the instrument with Galileo satellite signals PDOP is 1.04.

Ionosphere impact is small as Total Electron Content (TEC) is low and Ionospheric Index is also low (Fig. 4).

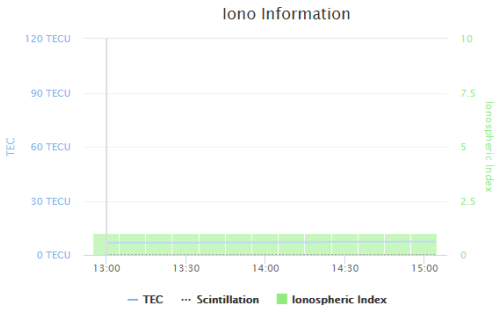

Fig. 4. Ionospheric information.

2. EXPERIMENTAL PART

When measurements are carried out under good conditions, with many satellites with good PDOP and a low ionosphere index, we can assume that these values have no effect. Further experiments are carried out to determine the accuracy of the measurements, the time to the FIX depending on the distance of the rover from the LatPos base station. Only a few stations on the LatPos system provide Galileo signal reception. Consequently, one base station, OJAR, has been used.

Two receivers have been used simultaneously for data acquisition and calculations. By placing two rover receivers side by side and measuring simultaneously, the same conditions are ensured: satellite positioning, ionosphere, satellite visibility, PDOP, and other conditions. Correction data are received from LatPos system in the same way. This ensures that the exact differences that result from measurements with and without Galileo satellite signals will be displayed.

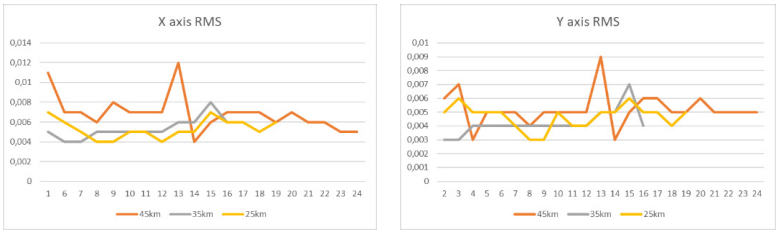

Fig. 5. X and Y coordinate RMS with different baseline length.

Taking into account the general assumption that correction errors up to 10 km from the base station are identical in both the rover receiver and the base station and the assumption that the baseline should not exceed 35 km to provide real-time online measurements, the following distances to the base station have been selected: 25 km, 35 km and 45 km [4]. The longest baseline has been selected over 35 km to ensure that measurements with baselines above 35 km could be performed using the Galileo signal. X and Y coordinate RMS measurements without Galileo satellite signal (Fig. 6) are increasing only few millimetres with a longer baseline (Fig. 5).

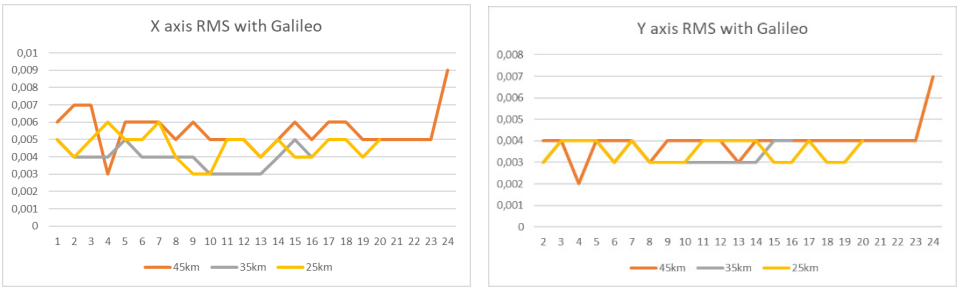

Fig. 6. Coordinate RMS using Galileo signal in calculations.

The instrument receiving the Galileo signal reduces the mean quadratic error of the measurements and is more stable. This means that the Galileo signal provides increased accuracy and stability of measurements. As measurement weights fall within the error limits, measurement stability is a major consideration.

The additional reception of Galileo satellites increases the number of satellites, resulting in a more homogeneous distribution and lower PDOP. As it is shown in Fig. 7, PDOP value decreases by about 20 % and it ensures an increase in measurement accuracy.

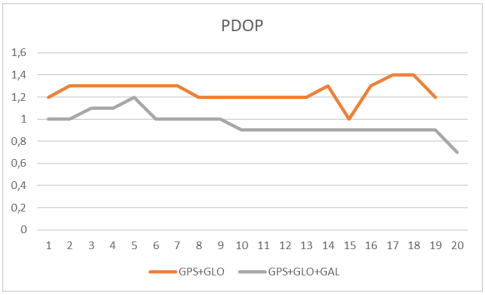

Fig. 7. Satellite PDOP changes in time.

As the distance from the base station to longer baselines increases, the time to the FIX position should increase as the rover instrument has other measurement conditions – the ionosphere and the troposphere.

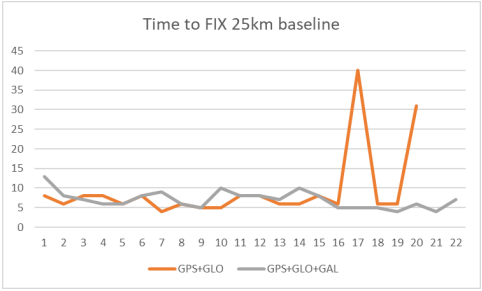

Fig. 8. Time to FIX on 25 km baseline.

Only by increasing the distance from 25 km to 35 km it can be observed that the average size does not change for 9 seconds. Measuring 45 km from the base station, the fixation time is even reduced (Figs. 9 and 10).

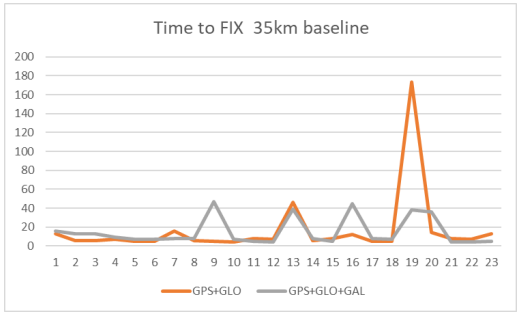

Fig. 9. Time to FIX on 35 km baseline.

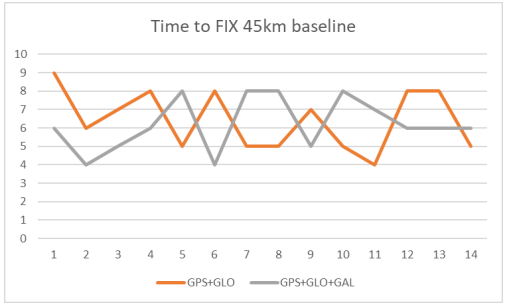

Fig. 10. Time to FIX on 45km baseline.

3. CONCLUSIONS

Having conducted the research, the following conclusions can be drawn:

- Galileo satellite system signal increases the number of satellites providing multiple measurements to satellites;
- The number of satellites increases by adding Galileo satellites, the PDOP improves by at least 20 %;
- Coordinate accuracy improves within error limits and remains independent of distance to base station, even when measuring on baseline longer than 35 km;
- Using Galileo satellite signals, the RMS of the measurements is reduced and becomes more stable. This increases the reliability of the measurements;
- When moving away from the base station, the time to fix increases by only 10 %. This means that the biggest factor for fixation time is the continuous and uninterrupted flow of correction data. Even on the longest baseline – 45 km, time to fix is shortest.

REFERENCES

1. Luo, X., Chen, J., & Richter, B. (2017). How Galileo Benefits High-Precision RTK. *GPS World*. Available at https://www.gpsworld.com/how-galileo-benefits-high-precision-rtk/
2. Zvirgzds, J. (2012). *Rational System LatPos*. Doctoral Thesis. Riga: Riga Technical University.
3. Norin, D., Öberg, S., & Stedt, F. (2017). Test measurements by Lantmäteriet with RTK and Galileo in SWEPOS. Lantmäteriet, *Rapportserie: Geodesi och Geografiska informationssystem*, 1–7.
4. Feng, Y., & Wang, J. (2001). *Exploring GNSS RTK Performance Benefits with GPS and Virtual Galileo Measurements*. www.researchgate.net/publication/241755023
5. Chen, X., Vollath, U., Landau, H., & Sauer, K. (2004). *Will GALILEO/Modernized GPS Obsolete Network RTK?* https://www.researchgate.net/publication/229039808.

GNSS RTK VEIKTSPĒJAS UZLABOJUMI, IZMANTOJOT GALILEO SATELĪTA SIGNĀLU

J. Zvirgzds, A. Celms

K o p s a v i l k u m s

Divi GNSS reālā laika kinemātiskās (RTK) pozicionēšanas faktori ir atkarība no attāluma līdz bāzes stacijai un slikti novērošanas apstākļi pilsētās vai mežā. Daudzfrekvences GNSS signālu un sistēmu izmantošana, iespējams, varētu uzlabot RTK pakalpojumus LatPos sistēmā, reģionālā un globālā mērogā. Precīzāki mērījumi no vairākām satelītu sistēmām, piemēram, NAVSTAR, Galileo, Glonass un BeiDou, var uzlabot RTK mērījumu rezultātu veikšanu attiecībā uz precizitāti, pieejamību, uzticamību un laiku līdz fiksācijai. Ieguvumi no vairākām GNSS pakalpojumu sistēmām ir šādi: 1) stacijas infrastruktūras izmaksu samazinājums; 2) RTK precizitātes un uzticamības uzlabošana profesionāliem lietotājiem. Darba mērķis ir izpētīt kā darbojas RTK sistēma, izmantojot vairākas satelīta sistēmas, pievienojot Galileo signāla mērījumus. Galileo mērījumi tiek novēroti, izmantojot lauka uztvērēju un korekcijas, kas saņemtas no LatPos bāzes staciju tīkla. Skaitliskā analīze tiek veikta, izmantojot reāllaika korekcijas lauka uztvērējos, un iegūtos RINEX datu rezultātus salīdzina dažādas skaitļošanas shēmas, piemēram, L1 / L2 signālus, NAVSTAR un NAVSTAR, ar Galileo mērījumiem. Rezultāti provizoriski parādīja būtisku uzlabojumu, izmantojot abus GNSS satelīta signālus. Darbā ieviesti turpmāki LatPos sistēmas uzlabojumi un parādīti plānotie uzlabojumi.

Atslēgas vārdi: *Galileo, globālā satelītu navigācijas sistēma, satelīta signāls*